Hard-X-ray-selected Active Galactic Nuclei – II. Spectral Energy Distributions in the 5-45 GHz domain

Francesca Panessa[1]*, Elia Chiaraluce[2], Gabriele Bruni[1], Daniele Dallacasa[3,4], Ari Laor[5], Ranieri D. Baldi[4], Ehud Behar[5], Ian McHardy[6], Francesco Tombesi[7,8,9,10,11], Fausto Vagnetti[1,7]

[1] *INAF – Istituto di Astrofisica e Planetologia Spaziali, via del Fosso del Cavaliere 100, I-00133 Roma, Italy*
[2] *AKKA Technologies Italia srl, via Tiburtina 1072/1074, 00156 Roma, Italy*
[3] *DiFA – Dipartimento di Fisica e Astronomia, Università di Bologna, via P. Gobetti 93/2, I-40129 Bologna, Italy*
[4] *INAF – Istituto di Radioastronomia, via Piero Gobetti 101, I-40129 Bologna, Italy*
[5] *Physics Department, The Technion, 32000, Haifa, Israel*
[6] *School of Physics and Astronomy, University of Southampton, Southampton, SO17 1BJ, UK*
[7] *Dipartimento di Fisica, Università di Roma "Tor Vergata", Via della Ricerca Scientifica 1, I-00133 Roma, Italy*
[8] *INAF – Astronomical Observatory of Rome, Via Frascati 33, I-00078 Monte Porzio Catone, Italy*
[9] *Department of Astronomy, University of Maryland, College Park MD 20742, USA*
[10] *X-ray Astrophysics Laboratory, NASA/Goddard Space Flight Center, Greenbelt, MD 20771, USA*
[11] *INFN – Roma Tor Vergata, Via della Ricerca Scientifica 1, 00133, Roma, Italy*

22 June 2022

ABSTRACT

A wide-frequency radio study of Active Galactic Nuclei (AGN) is crucial to evaluate the intervening radiative mechanisms responsible for the observed emission and relate them with the underlying accretion physics. We present wide frequency (5-45 GHz), high-sensitivity (few μJy beam^{-1}), (sub)-kpc JVLA observations of a sample of 30 nearby ($0.003 \leqslant z \leqslant 0.3$) AGN detected by *INTEGRAL/IBIS* at hard-X-ray. We find a high detection fraction of radio emission at all frequencies, i.e. $\geqslant 95$ per cent at 5, 10 and 15 GHz and $\geqslant 80$ per cent at 22 and 45 GHz. Two sources out of 30 remain undetected at our high sensitivities. The nuclear radio morphology is predominantly compact, sometimes accompanied by extended jet-like structures, or more complex features. The radio Spectral Energy Distributions (SEDs) of the radio cores appear either as single or as a broken power-law, a minority of them exhibits a peaked component. The spectral slopes are either flat/inverted or steep, up to a break/peak or over the whole range. The sample mean SED shows a flat slope up to 15 GHz which steepens between 15 and 22 GHz and becomes again flat above 22 GHz. Significant radio-X-ray correlations are observed at all frequencies. About half of the sample features extended emission, clearly resolved by the JVLA, indicating low-power jets or large scale outflows. The unresolved cores, which often dominate the radio power, may be of jet, outflow, and/or coronal origin, depending on the observed frequency.

Key words: galaxies: active –galaxies: nuclei – galaxies: jets – galaxies: Seyfert – black hole physics – radio continuum: galaxies

1 INTRODUCTION

The connection between the accretion and ejection physics in Active Galactic Nuclei (AGN) has been one of the hot topics of extragalactic astrophysics since the first discoveries of active galaxies. The existence of scaling relations involving the black-hole mass and fundamental quantities related to the host galaxy (e.g. Kormendy & Richstone 1995; Magorrian et al. 1998; Ferrarese & Merritt 2000; Gültekin et al. 2009) suggests that the AGN ejection activity and host galaxy evolution are entangled. Indeed, the mechanical kinetic energy ejected by the jet is believed to be one source

of AGN feedback into the host galaxy (Morganti 2017). A connection between the accretion and the ejection phenomena, with analogous properties to AGN, has been observed in other accreting systems like black-hole X-ray binaries, XRB (e.g. Falcke et al. 2004), coronally-active stars (e.g. Laor & Behar 2008; Raginski & Laor 2016), young stellar objects (e.g. Price et al. 2003; Ferreira & Deguiran 2013), cataclysmic variables (e.g. Körding et al. 2008), ultra–luminous X-ray sources (e.g. Mezcua et al. 2013) and tidal disruption events (e.g. Zubovas 2019), suggesting a common underlying physics.

Historically, AGN has been divided between Radio-Loud

---

* Contact e-mail:francesca.panessa@inaf.it

(RL) and Radio-Quiet (RQ)[1]. However, the radio-loudness definition strongly depends on the observed frequency, on the region size from where the radio flux is measured, and the boundaries between RL and RQ AGN may also depend on the accretion rate and luminosity of the source Panessa et al. (2007). Padovani (2016) proposed a more physically meaningful dichotomy between 'jetted' and 'non-jetted' sources, where 'jetted' sources are those exhibiting a clear signature of a relativistic jet. In this work we refer to RQ AGN in the sense of 'non-jetted' sources. There is emerging evidence that RQ AGN are not radio-silent, as in these objects we do observe radio emission in a variety of shapes, scales and strengths, with sources exhibiting outflowing and jet-like features, sub-relativistics, less powerful, less collimated and on smaller scales with respect to those of powerful RL AGN (e.g. Nagar et al. 2002), see Panessa et al. (2019) for a review.

Previous works focusing on the cm spectral range of the RQ population at arcsec resolution generally reported moderately-to-high detection fractions, i.e. 70 - 90 per cent (e.g. van der Hulst et al. 1981; Kukula et al. 1995; Roy et al. 1998; Nagar et al. 1999; Thean et al. 2000). More recently, Smith et al. (2016, 2020) found a high detection fraction (∼96 per cent) for a sample of hard-X-ray selected AGN from Swift/BAT at 22 GHz with a ∼1 arcsec resolution.

The morphology of the radio emission on arcsec scales is predominantly compact, either unresolved or marginally resolved. However, a number of sources exhibit extended structures, linear features, double/triple components, core plus jet like features as well as diffuse emission, on spatial scales ranging from ∼kpc (e.g. Ulvestad et al. 1981; Kukula et al. 1998; Leipski et al. 2006) down to few hundreds of pc (e.g. Kukula et al. 1995; Schmitt et al. 2001; Thean et al. 2001).

Previous studies of the spectral shape of RQ AGN were mainly performed at frequencies ⩽15 GHz, usually adopting a two-frequencies approach, which only gives a limited information on the overall shape due to the limited frequency coverage (e.g. Kellermann et al. 1989; Kukula et al. 1998; Chen et al. 2022). Only few works have adopted a multi-frequency approach to study the spectral shape of RQ AGN, but still limited to the frequency range ν ⩽15 GHz (e.g. Antonucci & Barvainis 1988; Barvainis et al. 1996; Kukula et al. 1998; Barvainis et al. 2005). These works have led to the finding that most sources show only steep spectra, however a number of them (roughly 40-50 per cent) exhibit flat/inverted spectra in the cm/sub-cm range (e.g. Antonucci & Barvainis 1988; Kukula et al. 1995; Barvainis et al. 1996; Kukula et al. 1998; Barvainis et al. 2005; Laor et al. 2019; Chiaraluce et al. 2019).

In a number of sources the flat/inverted slope is found to dominate only at higher frequencies (⩾ few GHz), i.e. an excess emission is found with respect to the extrapolation from lower frequencies. This trend has been first reported as a "high-frequency excess" up to 2 cm by Antonucci & Barvainis (1988); Barvainis et al. (1996), and then as a mm-

excess, up to ∼ 100 GHz, by Laor & Behar (2008); Behar et al. (2015, 2018). Several radiative processes have been invoked to explain the evidence of flat/inverted cm/sub-cm spectra in RQ AGN, both thermal and non-thermal, like optically-thick synchrotron emission from a compact source, either the base of the jet (e.g. Falcke et al. 1995; Wilson & Colbert 1995; Baldi et al. 2021a, 2022) or a magnetically-heated corona (e.g. Laor & Behar 2008; Raginski & Laor 2016), thermal free-free emission from nuclear sources at $T_B \sim 10^6$ K and $T_B \sim 10^4$ K emission from NLR or starburst (e.g. Antonucci & Barvainis 1988; Barvainis et al. 1996; Padovani et al. 2011; Condon et al. 2013).

The evidence of steep spectra in RQ AGN has been explained invoking synchrotron or free-free emission in the optically-thin regime from disk or circumnuclear starburst regions, on host-galaxy scale but also down to few hundreds pc (e.g. Barvainis et al. 1996; Padovani et al. 2011; Condon et al. 2013; Zakamska et al. 2016); optically-thin synchrotron from AGN-driven outflows, usually on few kpc scale (e.g. Mundell et al. 2000; Jiang et al. 2010; Zakamska & Greene 2014; Laor et al. 2019); or optically-thin synchrotron emission from plasma blobs in a sub-relativistic jet, usually associated to a linear morphology and on scales as small as hundreds of pc (e.g. Barvainis et al. 1996; Kukula et al. 1999; Laor et al. 2019).

As additional research channel, the study of correlations between the X-ray luminosity, considered a proxy for the accretion power, and the radio one, measuring the strength of ejection phenomena, has allowed to test different physical scenarios, such as radiatively efficient versus inefficient regimes (e.g. Merloni et al. 2003; Falcke et al. 2004; Coriat et al. 2011; Dong et al. 2014; Dong & Wu 2015), or the so-called coronal models (e.g. Laor & Behar 2008; Raginski & Laor 2016).

This work is a completion of the results presented in Chiaraluce et al. (2020), which we hereafter refer to as Paper I. Here, we present the results from new Jansky Very Large Array (JVLA) multi-frequency observations and Spectral Energy Distributions (SEDs) for a sample of hard-X-ray selected AGN, in a wide range of frequencies, 5 - 45 GHz, with a high sensitivity, few μJy/beam, and at a resolution of ∼ arcsec, i.e. spatial scales ⩽kpc.

In this paper we use the Λ-CDM with the following cosmological parameters: H_o=67.4 km s^{-1} Mpc^{-1}, Ω_m=0.315 and Ω_Λ=0.685 (Aghanim et al. 2018).

2 THE SAMPLE

The starting point of our project is the volume limited sample of 89 hard-X-ray selected AGN observed by INTE-GRAL/*IBIS* and presented in Malizia et al. (2009). We selected only the sources conveniently observable with the JVLA between 5 and 45 GHz, i.e. north of DEC -30 deg, and we considered only Seyfert galaxies, criteria which reduce the sample to 44 objects (hereafter 'parent' sample). The characteristics of this sample have been extensively presented in Paper I, and are here briefly retrieved.

This hard-X-ray selected sample has several advantages: i) the hard-X-ray selection makes it relatively free of selection biases, e.g. absorption (see discussion in Ho & Ulvestad 2001, and Paper I); ii) it comprises moderate-to-high luminosity objects, with $41.5 \leqslant \log L_{2-10\,\mathrm{keV}}\ (erg\,s^{-1}) \leqslant 44.5$; iii) the ac-

---

[1] The RL/RQ definition is based on the value of the ratio of optical-to-radio fluxes $R_O = \log \frac{f(4400\text{Å})}{f(6\,cm)}$ (Kellermann et al. 1989). A similar definition has been proposed considering the radio-to-X-ray luminosities: $R_X = \log (L_R(6\,cm)/L_{2-10\,\mathrm{keV}})$, with -4.5 as dividing threshold between RQ and RL (e.g. Terashima & Wilson 2003; Panessa et al. 2006)

cretion rates are relatively high: $-2.5 \leqslant \log \mathrm{L_{Bol}}/L_{Edd} \leqslant -0.5$ (central panel of Fig. 1); iv) it covers a wide range of radio luminosities (Fig. 2), with the bulk of the population made of RQ AGN (Fig. 3).

3 RADIO OBSERVATIONS AND DATA REDUCTION

In the present work we couple our high-frequencies radio data at 22 and 45 GHz (JVLA-C configuration, project 18B-163, ~ 1 and $0.5''$ resolution, respectively) already published in Paper I, to lower frequencies (5, 10 and 15 GHz, i.e., C, X and Ku bands respectively) proprietary data obtained in JVLA-B configuration (project: 19A-018). The more extended configuration at lower frequencies guarantees us a matched resolution with high frequencies data, a crucial point in order to build physically meaningful SEDs: at 5, 10 and 15 GHz the expected resolution is ~ 1, 0.6 and $0.4''$. Moreover, we complemented the high-frequency observations at 22 and 45 GHz with new ones obtained in the same configuration (project 20A-066).

Finally, we searched in the VLA archive low-frequency data for the objects for which our own proprietary data were not available (i.e. NGC 788, NGC 1068, QSO B0241+62, NGC 1142, B3 0309+411B, MCG +08-11-11, Mkn 3 and Mkn 6). When available, we selected observations in the same configurations (VLA-B), when not we considered other available configurations (mostly A), and in order to match the resolution a tapering has been applied (next Section).

The above strategy translates into 30 objects out of 44 with at least two SED data points. In Table 1 we summarise the characteristics of the sample together with information on the observations and the corresponding projects: 9 sources have only two SED data points; one source (Mkn 50) has three SED data points; two sources have four data points (NGC 788 and B3 0309+411B), the majority of sources (18 out of 30) have 5 SED data points.

In Fig. 1 we plot a histogram of the distribution of the relevant physical quantities of sources in this work, i.e redshift, Eddington ratio and X-ray radio-loudness ($\mathrm{R_X} = \log\,(\mathrm{L_R}\,(6\,\mathrm{cm})/\mathrm{L_{2-10\,keV}})$), as compared to the whole sample of 44 source north DEC $\geqslant$ -30 deg. A Kolmogorov-Smirnov test comparing the two distributions results, in all cases, in a P$\sim$0.99, so the null hypothesis that the two samples are drawn from the same parent population cannot be rejected. This would suggest that the physical conclusions which can be drawn from the sources considered in this work are likely representative of the whole sample.

The project 19A-018 has been observed in the period February - May 2019, the project 20A-066 in the period February - May 2020. The characteristics of observations for the high-frequency project 20A-066 are the same of 18B-163, presented in Section 3 of Paper I, and we refer to that section for the details. Sources in 19A-018 were observed at 5, 10 and 15 GHz for a minimum of 1 min to a maximum of 5 min. We applied phase calibration, bracketing targets with suitable sources within a radius of 10 deg. The scans of the absolute flux density scale calibrator has been performed once per scheduling block, typically at the beginning or end of it, and, at a given frequency, it is observed for no less than 2min30s.

The data calibration and reduction procedure for the proprietary JVLA data has been performed with the calibration pipeline within the Common Astronomy Software Application (CASA 5.4.1 version[2], McMullin et al. 2007). After calibration, the plots were inspected for residual RFI. For the image reconstruction, the TCLEAN task in CASA has been used, applying the Högbom (1974) deconvolver. We produced full resolution maps considering as initial weighting the Briggs (1995) one with robustness parameter equal to 0.5, which ensures a balance between resolution and sensitivity. However, in order to have X and Ku maps at a matched resolution with respect to C band, we produced naturally-weighted tapered maps, in order to give more weight to the short baselines and have an approximately equal UV coverage.

The typical RMS achieved is $\sim 10 - 40\,\mu\mathrm{Jy\,beam^{-1}}$, in agreement with proprietary post-upgrade JVLA data (see Table 3 in Supplementary material). For the archival VLA data, the reduction has been performed with the Astronomical Image Processing System AIPS in the 31DEC20 version[3], following standard procedures. The imaging procedure has been conducted via the task IMAGR. In all cases, self–calibration has been performed for all the sources strong enough to provide enough flux density for the model.

For both the proprietary JVLA data and the archival VLA ones, the image analysis has been performed via the CASA task IMFIT. Based on the source morphology, single/multiple Gaussian fit on the image plane has been performed. A comparison of the flux densities of calibrators for the proprietary JVLA data with tabulated values in Perley & Butler (2017) led to the estimation of a $\sim$5 per cent error in the flux calibration; for the archival data a more conservative 10 per cent has been adopted. The uncertainties in the final flux density measurements are affected by fitting errors from IMFIT, and flux calibration error, which are added in quadrature and adopted as the error measurements. In the case of components with a resolved morphology, the error associated with the flux determination is given by the formula $\sigma_S = \sqrt{N \times (rms)^2 + (A_s \times S)^2}$, where N is the number of beam areas covered by a source of flux density S, and A_S takes into account the uncertainty in the absolute flux density scale (0.05$-$0.1, see Ho & Ulvestad 2001).

In Table 1 we report the source coordinates taken from Malizia et al. (2009). In a number of sources the above positions display a significant offset from the derived radio ones (the latter reported in Table 3 in Supplementary material). For this reason, we performed a careful cross-check with all available positions (from optical, X-ray, IR, etc observations) in literature[4] for each source, in order to determine the likely core component. In the maps, the white (or black) crosses represent the original optical coordinates as in Malizia et al. (2009), as quoted in Table 1, that were adopted during the scheduling of our observations and therefore are their phase centres. In Table 2 in Supplementary material we report the integrated and peak radio luminosities of the core component at all frequencies and in Table 3 in Supplementary material we report the derived parameters from the imaging analysis. The complete set of maps for the entire sample is available

---

[2] https://casa.nrao.edu
[3] http://www.aips.nrao.edu
[4] With the NASA NED and SIMBAD databases.

Table 1. List of sources together with observations information. *Columns:* (1) Target name; (2) and (3) Right ascension and declination (J2000) from Malizia et al. (2009); (4) Seyfert type; (5) Redshift; (6), (7), (8), (9) and (10), C, X, Ku, K and Q band projects, respectively. For the archival data we use the following notation: VLA project (month/year) [VLA configuration].

					Observations				
Target	RA (J2000)	DEC (J2000)	Seyfert Type	z	C (5 GHz)	X (10 GHz)	Ku (15 GHz)	K (22 GHz)	Q (45 GHz)
(1)	(2)	(3)	(4)	(5)	(6)	(7)	(8)	(9)	(10)
IGR J00333+6122	00:33:18.41	+61.27.43.10	S1.5	0.105	$\cdots$	$\cdots$	$\cdots$	18B-163	18B-163
NGC 788	02:01:06.40	−06:48:56.0	S2	0.0136	AW0126 (02/85) [A]	AM384 (12/92) [A]	$\cdots$	18B-163	18B-163
NGC 1068	02:42:40.71	−00:00:47.8	S2	0.0038	BG066 (04/99) [B]	AZ0053 (04/92) [C]	AW0085 (01/84) [B]	18B-163	18B-163
QSO B0241+62	02:44:40.71	+62.28.06.5	S1	0.044	AM0124 (06/86) [B/A]	AS644 (11/98) [C]	AS0786 (04/04) [C]	18B-163	18B-163
NGC 1142	02:55:12.19	−00.11.02.3	S2	0.0288	12A-066 (06/12) [B]	AP233 (06/91) [A] AP212 (04/92) [B]	AJ105 (05/84) [B]	18B-163	18B-163
B3 0309+411B	03:13:01.96	+41.20.01.2	S1	0.136	BT0007 (05/94) [A/B]	BM0074 (04/97) [B]	$\cdots$	18B-163	18B-163
NGC 1275	03:19:48.16	+41.30.42.1	S2	0.0175	$\cdots$	$\cdots$	$\cdots$	18B-163	18B-163
LEDA 168563	04:52::04.85	+49.32.43.7	S1	0.029	$\cdots$	$\cdots$	$\cdots$	18B-163	18B-163
4U 0517+17	05:10:45.51	+16.29.55.8	S1.5	0.0179	$\cdots$	$\cdots$	$\cdots$	18B-163	18B-163
MCG+08-11-11	05:54:53.61	+46.26.21.6	S1.5	0.0205	ULVE (03/82) [A]	AB0973 (11/04) [A]	AU0018 (11/83) [A]	18B-163	18B-163
Mkn 3	06:15:36.36	+71.02.15.1	S2	0.0135	AW0258 (08/90) [A] GK0011 (02/94) [B]	AW0278 (09/91) [A] BM0124 (06/00) [B]	AP0142 (09/87) [A]	18B-163	18B-163
Mkn 6	06:52:12.25	+74.25.37.5	S1.5	0.0188	AB0740 (07/95) [A] AB0740 (11/95) [B] AB0740 (05/95) [D]	AW0278 (09/91) [A]	AP0142 (10/87) [A]	18B-163	18B-163
NGC 4151	12:10:32.58	+39:24:20.6	S1.5	0.0033	$\cdots$	$\cdots$	$\cdots$	18B-163	18B-163
Mkn 50	12:23:24.14	+02.40.44.8	S1	0.0234	19A-018	19A-018	19A-018	$\cdots$	$\cdots$
NGC 4388	12:25:46.75	+12.39.43.5	S2	0.0084	19A-018	19A-018	19A-018	18B-163	18B-163
LEDA 170194	12:39:06.32	-16.10.47.8	S2	0.036	19A-018	19A-018	19A-018	20A-066	20A-066
NGC 4593	12:39:39.42	-05.20.39.3	S1	0.009	19A-018	19A-018	19A-018	20A-066	20A-066
IGR J13091+1137	13:09:05.60	+11.38.02.9	S2	0.0251	19A-018	19A-018	19A-018	20A-066	20A-066
NGC 5252	13:38:16.00	+04.32.32.5	S2	0.023	19A-018	19A-018	19A-018	18B-163	18B-163
NGC 5506	14:13:14.87	-03.12.26.9	S1.9	0.0062	19A-018	19A-018	19A-018	20A-066	20A-066
IGR J16385-2057	16:38:30.91	-20.55.24.6	NLS1	0.0269	$\cdots$	$\cdots$	$\cdots$	20A-066	20A-066
IGR J16426+6536	16:43:04.70	+65:32:50.9	NLS1	0.323	$\cdots$	$\cdots$	$\cdots$	18B-163 20A-066	18B-163 20A-066
IGR J17513-2011	17:51:13.62	-20.12.14.6	S1.9	0.047	19A-018	19A-018	19A-018	20A-066	20A-066
IGR J18027-1455	18:02:45.50	-14.54.32.0	S1	0.035	$\cdots$	$\cdots$	$\cdots$	20A-066	20A-066
IGR J18259-0706	18:25:57.58	+07.10.22.8	S1	0.037	19A-018	19A-018	19A-018	20A-066	20A-066
2E 1853.7+1534	18:56:01.28	+15.38.05.7	S1	0.084	$\cdots$	$\cdots$	$\cdots$	20A-066	20A-066
IGR J20186+4043	20:18:38.73	+40.40.59.9	S2	0.0144	19A-018	19A-018	19A-018	20A-066	20A-066
4C +74.26	20:42:37.30	+75.08.02.4	S1	0.104	19A-018	19A-018	19A-018	20A-066	20A-066
IGR J23308+7120	23:30:37.28	+71.22.46.0	S2	0.037	19A-018	19A-018	19A-018	20A-066	20A-066
IGR J23524+5842	23:52:22.11	+58.45.30.7	S2	0.164	19A-018	19A-018	19A-018	20A-066	20A-066
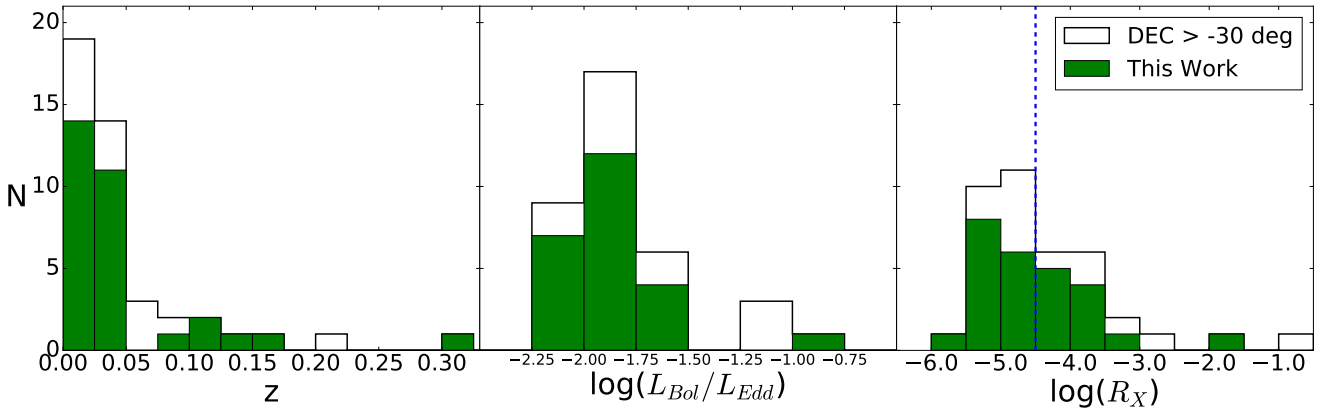
Figure 1. Histogram showing the distribution of redshift (from Malizia et al. 2009, left panel). Eddington ratio (L_{Bol}/L_{Edd}, centre panel) and radio-loudness parameter (from quantities tabulated in Panessa et al. 2015, right panel) for the parent sample (DEC > -30 deg, semi-filled histogram) and for the sources considered in this work (green), i.e. having at least two SED data points. The blue, vertical dashed line is the R_X = -4.5 limit of Terashima & Wilson (2003).

on the project's website[5], while a representative image for each source, together with its SED, is reported in Figure 2 in Supplementary material. In Table 2 we report the X-ray (2-10 keV and 10-100 keV) and bolometric luminosities and the corresponding Eddington ratios (as detailed in Paper I). The optical radio-loudness parameter (Kellermann et al. 1989) and the X-ray radio-loudness parameter (Terashima &

[5] https://sites.google.com/inaf.it/hxagn/radio-images

Table 2. Luminosities and radio loudness parameters: *Columns:* (1) Target name; (2) 2-10 keV X-ray luminosity Malizia et al. (2009); (3) 20-100 keV X-ray luminosity from Malizia et al. (2009); (4) Bolometric luminosity; (5) Eddington ratio; (6) Optical radio-loudness parameter (Kellermann et al. 1989); (7) X-ray radio-loudness at 5 GHz; (8) X-ray radio-loudness at 22 GHz; (9) X-ray radio-loudness at 45 GHz.

Name	$\log(L_{2-10\ keV})$ (erg/s)	$\log(L_{20-100\ keV})$ (erg/s)	$\log(L_{Bol})$ (erg/s)	$\log(L_{Bol}/L_{Edd})$	$\log(R_O)$	$\log(R_X^{5\ GHz})$	$\log(R_X^{22\ GHz})$	$\log(R_X^{45\ GHz})$
(1)	(2)	(3)	(4)	(5)	(6)	(7)	(8)	(9)
IGR J00333+6122	44.19	44.44	44.80	-1.84	1.90	-4.42	-4.64	-4.71
NGC 788	42.86	43.29	43.55	-2.06	-1.04	-5.42	-5.01	-4.9
NGC 1068	42.95	43.35	43.36	-1.95	0.04	-3.92	-4.11	-4.06
QSO B0241+62	43.87	44.41	44.39	-1.80	0.70	-3.06	-1.91	-1.60
NGC 1142	43.82	43.96	45.23	-2.27	0.08	-5.25	-4.88	-4.76
B3 0309+411B	45.04	44.99	$\cdots$	$\cdots$	3.28	-3.00	-1.96	-1.67
NGC 1275	42.89	43.38	44.32	-2.28	2.99	-0.96	-0.35	-0.16
LEDA 168563	43.9	44.04	44.33	-1.77	1.50	-4.70	-4.80	-4.80
4U 0517+17	43.23	43.62	43.44	-1.66	$\cdots$	-5.27	-4.75	-4.40
MCG+08-11-11	43.69	43.74	43.90	-1.65	1.27	-4.25	-4.29	-3.98
Mkn 3	44.17	43.79	44.77	-2.03	1.03	-4.79	-5.03	-4.98
Mkn 6	43.27	43.57	44.27	-1.96	1.17	-3.93	-3.40	-3.31
NGC 4151	43.05	43.16	43.89	-1.91	0.60	-5.41	-4.84	-4.73
Mkn 50	43.05	43.2	43.66	-1.84	-1.02	-5.53	$\cdots$	$\cdots$
NGC 4388	43	43.54	43.16	-1.80	-0.80	-4.94	-5.05	-4.83
LEDA 170194	43.48	44.22	44.76	-2.24	0.30	-4.42	-3.67	-3.20
NGC 4593	42.8	43.09	43.12	-1.72	-1.86	-5.63	-4.95	-4.49
IGR J13091+1137	43.44	43.77	44.44	-2.16	-0.90	-5.49	-5.17	-5.08
NGC 5252	43.72	43.71	44.89	-2.21	0.60	-4.71	-4.39	-4.60
NGC 5506	42.83	42.85	42.96	-1.79	0.90	-3.91	-3.85	-3.77
IGR J16385-2057	43.02	43.39	43.26	-1.67	$\cdots$	$\cdots$	-4.37	-4.32
IGR J16426+6536	$\cdots$	45.97	$\cdots$	$\cdots$	$\cdots$	$\cdots$	$\cdots$	$\cdots$
IGR J17513-2011	43.4	44.1	43.09	-1.01	$\cdots$	-4.75	-4.29	-3.89
IGR J18027-1455	43.23	44.04	43.83	-1.83	$\cdots$	$\cdots$	<-5.46	<-4.97
IGR J18259-0706	43.19	43.66	$\cdots$	$\cdots$	$\cdots$	-4.99	-4.65	-4.37
2E 1853.7+1534	44.25	44.56	44.55	-1.70	$\cdots$	$\cdots$	-5.64	<-5.17
IGR J20186+4043	42.57	42.98	$\cdots$	$\cdots$	-0.67	-4.72	-4.62	-4.60
4C +74.26	44.75	45.04	45.76	-1.96	1.92	-3.20	-2.54	-2.45
IGR J23308+7120	42.8	43.55	$\cdots$	$\cdots$	-0.44	-5.16	<-5.11	<-4.28
IGR J23524+5842	44.41	44.85	$\cdots$	$\cdots$	1.12	-5.04	-5.22	<-4.67

Wilson 2003) is calculated using the radio luminosities at 5, 22 and 45 GHz.

4 RESULTS

4.1 Detection rates, radio luminosities and radio loudness

We find high detection rates of radio emission at all frequencies, with detection fractions which decrease with frequency, i.e. 21/21, 21/21, 19/19, 26/29 and 24/29 at 5, 10, 15, 22 and 45 GHz, respectively, which translate into rates of 96±8, 96±8, 95±8, 87±12 and 81±14, respectively[6].

In Fig. 2 we show the distribution of core radio luminosities for the sources in the sample at different frequencies. The bulk of sources has core radio luminosities in the range $37 \leqslant \log \nu L_{\nu}(\mathrm{erg\,s^{-1}}) \leqslant 40$, well below the values observed in radio galaxies (i.e., $\log \nu L_{\nu}(\mathrm{erg\,s^{-1}}) > 42$, Zirbel & Baum (1995)).
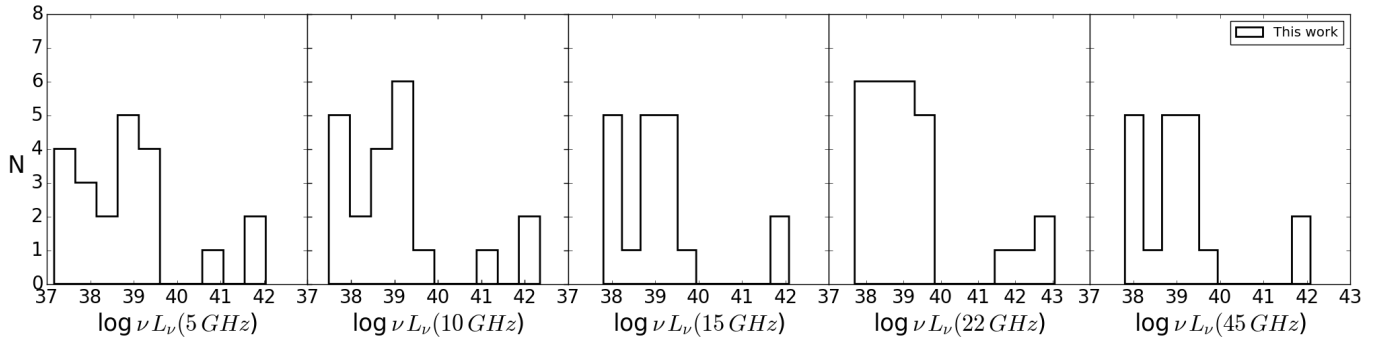
In Fig. 3 we show the distribution of radio-loudness parameters of the core component at different frequencies. The fraction of radio sources which can be classified as RL is 30 and 33 per cent considering the classical radio loudness parameter and the X-ray one at 5 GHz, respectively (Terashima & Wilson 2003). However, given the low radio luminosities

and the caveats associated to the definition of a boundary in the radio-loudness parameter, we consider as RQ AGN the majority of the sources in our sample, except for the three most powerful radio emitters already mentioned in Paper I, i.e. QSO B0241+62, B3 0309+411B and NGC 1275, and the giant radio galaxy 4C +74.26 (e.g. Bruni et al. 2020, and references therein), resulting in ∼ 13% of RL AGN in the sample. This fraction of RL AGN is consistent with what already observed so far in hard X-ray selected samples (e.g. Bassani et al. 2016, and references therein).

4.2 Undetected sources

Two sources out of 30 were not detected by our observations, i.e. IGR J16426+6536 and IGR J18027-1455, and for both only observations at 22 and 45 GHz were available. For both we give $3 \times \sigma$ upper limits of ∼0.1 and ∼0.15 mJy beam^{-1} at 22 and 45 GHz, respectively, which result, in the case of IGR J18027-1455, in upper limits on the radio luminosities of $\log L_R (\mathrm{erg\,s^{-1}}) \sim 37.8$ and 38.3 (upper limits on the radio powers of $L_{\nu}(\mathrm{W\,Hz^{-1}}) \sim 3 \times 10^{20}$ and $L_{\nu}(\mathrm{W\,Hz^{-1}}) \sim 4.5 \times 10^{20}$ at 22 and 45 GHz, respectively). The derived upper limits on the X-ray radio-loudness parameter are of -5.4 and -4.9 at the two frequencies, respectively, placing these sources at the very-low-power end of the radio-loudness distribution. The source IGR J16426+6536 benefits from observations in two epochs, one in November 2018 and presented in Paper I, and one in June 2020, presented here. In both cases the source is undetected at a similar flux limit (see Table 3 in Supplementary material), variability at

---

[6] Due to the limited statistics of the sample, in order to estimate the detection fractions and associated uncertainties we used the Laplace point estimate formula (Laplace 1812) and the Adjusted Wald method (e.g. Sauro & Lewis 2005).

Figure 2. Histogram showing the distribution of core radio luminosities $\log \nu L_\nu$ at the different frequencies for sources in the sample.
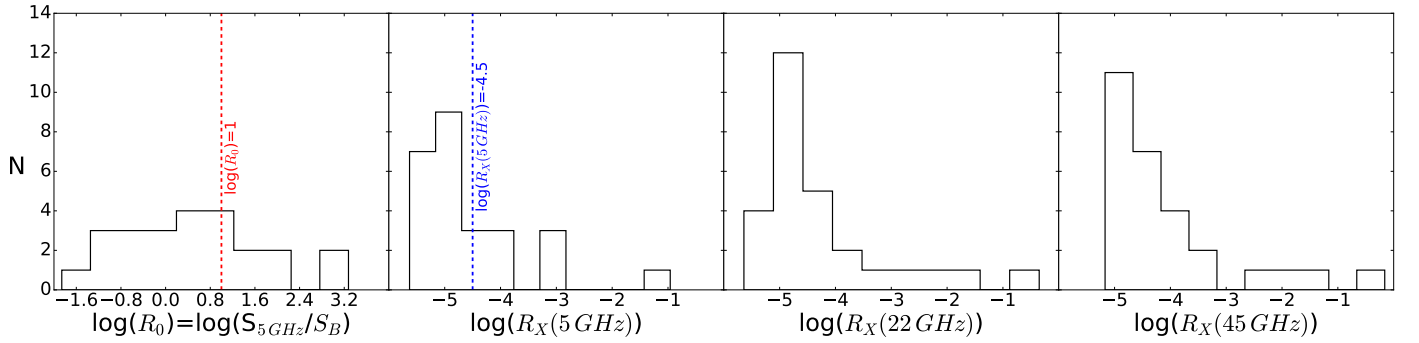
Figure 3. Histogram showing the distribution of radio loudness for the sources in the sample based on different definitions, i.e. Kellermann et al. (1989) (first panel, from left, 9/30 classify as RL); Terashima & Wilson (2003) at 5 GHz (second panel, 10/30 classify as RL), 22 GHz (third panel) and at 45 GHz (fourth panel). The vertical lines denote the RQ/RL limit depending on the definition.

17 months scales can therefore be ruled out. Deeper observations, achievable with longer integration times, would be required to confirm the radio-silent nature of these sources.
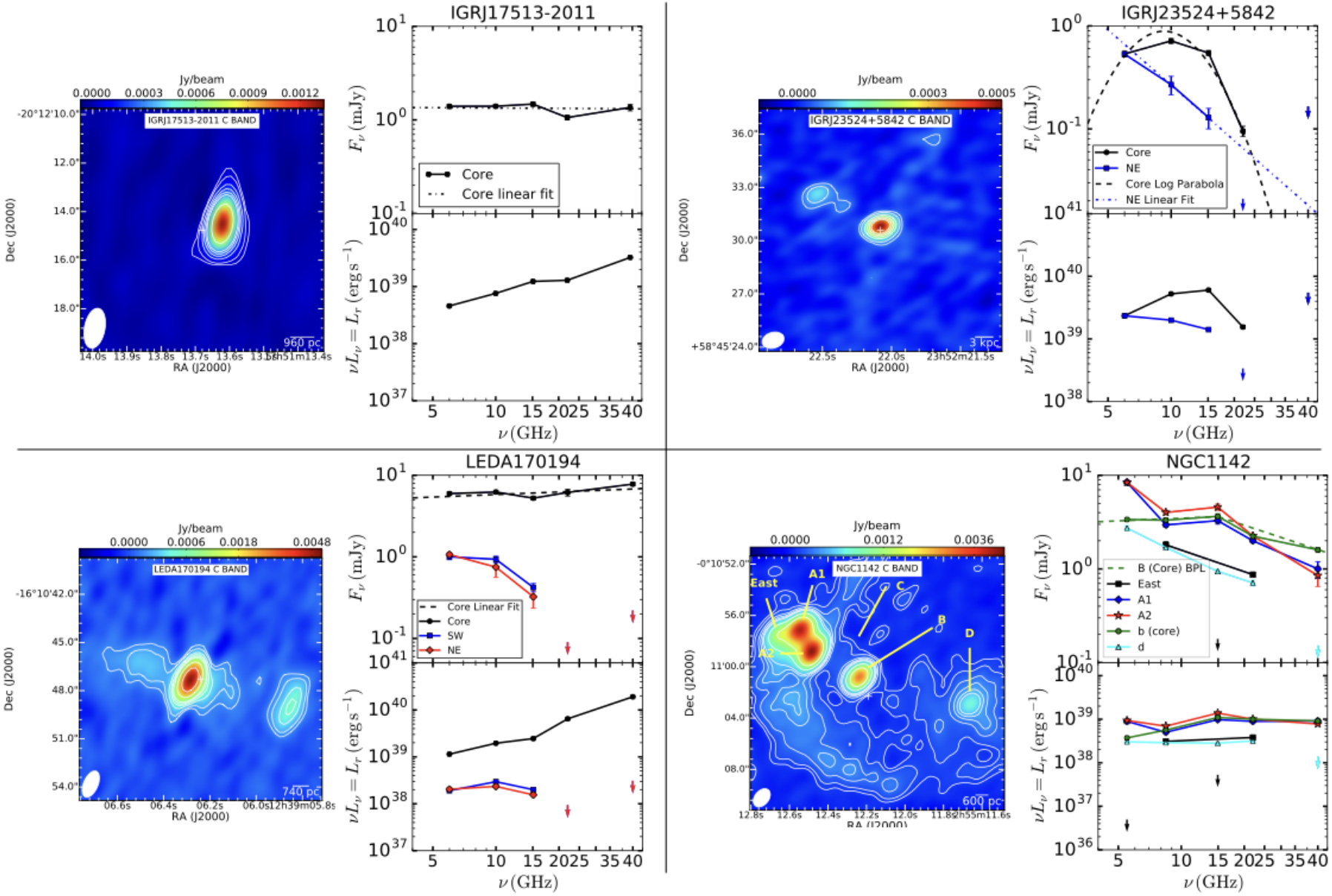
Figure 4. Radio maps of sources considered as an example for the four morphological types adopted in Section 4.3: top-left, IGR J17513-2011 (morphological class A); top-right, IGR J23524+5842 (morphological class B); bottom-left, LEDA 170194 (morphological class C); bottom-right, NGC 1142 (morphological class D). For space reasons, only the 5-GHz (C-band) maps are shown. For each source we also show the corresponding SED, in which we indicate the core and all the other emitting components (if present). The SED and morphology for the remaining sources are shown in Figure 2 in Supplementary material.

4.3 Morphology

We divided the morphology of the sources in the sample into four main classes, adapting the classification in Baldi et al. (2021b), considering both full array and tapered radio maps. In Table 3, we report the morphological classification (column 2) for each source and in Fig. 4 we report an examples of each of the four morphological classes:

• **core or core+jet/lobe (A)**: sources with a single core component, either resolved or marginally resolved, sometimes with a small-scale protrusion (either one-sided or two-sided); 17/30 sources belong to this class (e.g., IGRJ 17513-2011).
• **one-sided jet (B)**: sources with an extended asymmetric jet, which is possibly resolved into several emitting components at higher resolutions; 7/30 sources are in this class (e.g., IGRJ 23524+5842).
• **triple (C)** sources exhibiting a triple morphology, interpreted as the radio core plus symmetric jet/lobes (one source: LEDA 170194).
• **jet+complex (D)**: sources with a complex structure, with multiple components, either compact, diffuse and/or extended; three sources fall in this classification, i.e. NGC 1068, NGC 1142 and NGC 5506. Note that the D classification corresponds to the E classification in Baldi et al. (2021b).

The morphological study for the sources across the cm-wave range reveals a prevalence of compact components, either unresolved or marginally-resolved, with nearly a half of the sample sources exhibiting jet-like structures, as well as triple and more complex ones that extend up to kpc scales. We note that the morphological classification depends on the distance of the source, i.e., for high z sources structures below the kpc scales are not resolved. However the majority of the sample sources are located in the nearby Universe, allowing us to map projected linear sizes of hundreds of pc (e.g. the nearest source is NGC 4593, $\sim$ 190 pc). On the other hand, high z objects (z> 0.1) in our sample are mostly radio galaxies (e.g. 3C+74.26, $\sim$ 2 kpc) with a known morphology. The classification also depends on the selected frequency. As an example, MCG+08-11-11 appears as a core plus a one sided jet-like feature in our maps at matched resolution of $\sim$1 arcsec, however, in the full resolution image, the core is resolved into 3 components, the central one being the core (e.g. Ulvestad & Wilson 1986). Indeed, sources with extended emission are best detected at low frequencies for a combination of effects. The surface brightness is enhanced by the steep spectrum and for a given JVLA configuration, the beam is larger, increasing the sensitivity to low surface brightness emission.

4.4 Radio spectral energy distributions

With the present observations, spanning the 5 - 45 GHz interval, we can build spectral energy distributions in the cm/sub-cm range at a matched resolution ($\sim$ arcsec) and sensitivity (a few μJy beam^{-1}) for a statistically relevant sample. In this way it is possible to characterise the wide-frequency emission for the emitting components, both nuclear and extra-nuclear, and interpret them in light of models invoked for emission in RQ objects.

The definition of the spectral index used in this work is $S_\nu^I \propto \nu^{-\alpha}$, where S_ν^I is the integrated flux density. The uncertainties associated with the spectral indices has been es-timated as $\sqrt{(\sigma_{f_1}/S_{f_1})^2 + (\sigma_{f_2}/S_{f_2})^2}/ln(f_2/f_1)$, where $\sigma_{f_{1,2}}$ and $S_{f_{1,2}}$ are the uncertainties on the flux density and the flux density at the two frequencies (Ho & Ulvestad 2001), which are the central frequencies of the K and Q bands (therefore the flux densities are the mean across the bandwidth). We define a steep spectrum as having $\alpha \geqslant 0.5$, and a flat one as having $\alpha < 0.5$, as in (Panessa & Giroletti 2013). We define a spectrum as inverted if $\alpha < 0$.

In order to characterise the spectral shape of the core components, we adopted the classification presented in Barvainis et al. (1996), (see also Scheuer & Williams (1968)), i.e. single power-law (S) spectra, for which a simple power-law fit is sufficient, concave (C+) and convex (C-) spectra, for which the spectrum can be fitted by a quadratic polynomial, and complex spectra (CPX), which do not fit in none of the above cases. Based on the evidence in the sample, we add an extra class, the spectra for which a broken power-law (BPL) fit represents well the data.

In Table 4 we report the results of the SED fitting, first for the broken power-law sources, then for the convex sources and finally for the single power-law ones. In Fig. 2 in Supplementary material we show the spectral flux and energy distributions of sources across the frequency range covered by our observations (sources are ordered as in Table 4), while in Fig. 5 we show the distribution of two-frequency spectral indices for the core components of sources in the sample for the frequency pairs 5-10 GHz, 10-15 GHz, 15-22 GHz and 22-45 GHz. The relative fraction of sources in the different classes is the following: 67% of single power-law spectra (e.g. left panels of Fig. 4), 14% of convex spectra (e.g. top-right panel of Fig. 4), 19% of broken power-law spectra (e.g. bottom-left panel of Fig. 4), none of concave nor complex spectra. However, cases which have been classified as convex, i.e. NGC 4593 and IGR J13091+1137, could be classified in the complex class as well (see next sections). In this classifications we excluded the sources with less than 2 frequency points (6/30 with two data points, 1/30 with one and 2/30 undetected).

The extra-nuclear components, when present, generally exhibit steep spectra.

5 DISCUSSION

5.1 Detection rates of radio emission

The detection rates of radio emission we find here are generally higher with respect to values reported in literature for surveys of Seyfert galaxies, especially at lower frequencies, typical percentages 70−90 (e.g. van der Hulst et al. 1981; Antonucci & Barvainis 1988; Kellermann et al. 1989; Ulvestad & Wilson 1989; Kukula et al. 1995; Roy et al. 1998; Nagar et al. 1999; Thean et al. 2000; Smith et al. 2020; Silpa et al. 2020; Sebastian et al. 2020; Nyland et al. 2020; Baldi et al. 2021b). However, a comparison with these works is not straightforward for several reasons: i) the different selection criteria on which the various samples are based, which may led to selection biases; ii) the different resolution of the observations, which may result in comparison of different components because of the mismatch in the spatial scale; iii) the different frequency coverage, as at different frequencies emission from different components is expected to dominate, and the spectral shape may change; iv) the different sensitivity,

Table 3. The two-frequency spectral indices (and associated uncertainties) for the sources and the multiple components, when present. The frequency pairs considered are 5-10 GHz, 10-15 GHz, 15-22 GHz, 22-45 GHz; for NGC 788 and B3 0309+411B we report the 10-22 GHz spectral index, due to the lack of 15 GHz data. We also indicate the morphological classification based on the four classes.

Name	Radio morph	Component	α_{5-10}	α_{10-15}	α_{15-22}	α_{22-45}	α_{10-22}
IGR J00333+6122	A	core	$\cdots$			1.2 ± 0.4	
NGC 788	A	core	0.8 ± 0.2	$\cdots$	$\cdots$	0.4 ± 0.3	-0.05 ± 0.20
NGC 1068		a	0.65 ± 0.13	1.64 ± 0.13	0.69 ± 0.17	0.9 ± 0.1	
	D	b(core)	0.49 ± 0.13	1.59 ± 0.13	1.1 ± 0.2	0.8 ± 0.1	
		d	$\cdots$	$\cdots$	0.62 ± 0.18	0.47 ± 0.01	
		sw	$\cdots$	$\cdots$	-0.24 ± 0.19	0.14 ± 0.10	
QSO B0241+62	B	core	-0.86 ± 0.13	-1.34 ± 0.12	0.252 ± 0.180	0.3 ± 0.1	
		blob	0.57 ± 0.13	2.4 ± 0.2	$\cdots$	$\cdots$	
NGC 1142	D	east	$\cdots$	$\cdots$	$\cdots$	$\cdots$	
		a1	2.45 ± 0.18	-0.18 ± 0.18	1.28 ± 0.25	0.9 ± 0.3	
		a2	1.72 ± 0.17	-0.24 ± 0.16	1.83 ± 0.23	1.4 ± 0.1	
		b(core)	0.04 ± 0.17	-0.17 ± 0.15	1.26 ± 0.21	0.5 ± 0.1	
		d	1.11 ± 0.18	1.03 ± 0.12	0.73 ± 0.22	$\cdots$	
B3 0309+411B	B	core	-0.38 ± 0.13	$\cdots$	$\cdots$	0.06 ± 0.10	-0.7 ± 0.1
		nw	0.11 ± 0.13	$\cdots$	$\cdots$	$\cdots$	
NGC 1275	A	core	$\cdots$	$\cdots$	$\cdots$	0.4 ± 0.1	
LEDA 168563	A	core	$\cdots$	$\cdots$	$\cdots$	1.07 ± 0.12	
4U 0517+17	A	core	$\cdots$	$\cdots$	$\cdots$	-0.09 ± 0.11	
MCG+08-11-11	B/C	core	1.07 ± 0.13	1.1 ± 0.1	0.14 ± 0.19	0.7 ± 0.1	
		jet	2.23 ± 0.13	2.5 ± 0.5	-3.2 ± 0.9	1.1 ± 0.4	
Mkn 3		west	1.31 ± 0.13	0.77 ± 0.12	1.8 ± 0.3	1.2 ± 0.1	
	B	east(core)	1.41 ± 0.13	0.35 ± 0.10	1.3 ± 0.1	0.87 ± 0.09	
Mkn 6		N	0.98 ± 0.07	1.13 ± 0.10	$\cdots$	$\cdots$	
	B/C/D	S(core)	0.91 ± 0.07	1.0 ± 0.1	$\cdots$	$\cdots$	
		Ext-EW	2.6 ± 0.1	$\cdots$	$\cdots$	$\cdots$	
NGC 4151	A	core	$\cdots$	$\cdots$	$\cdots$	0.7 ± 0.1	
Mkn 50	A	core	-0.06 ± 0.20	0.03 ± 0.23	$\cdots$	$\cdots$	
NGC 4388	B(core)	NE	0.9 ± 0.1	0.8 ± 0.2	1.08 ± 0.20	0.27 ± 0.11	
		SW	0.8 ± 0.1	0.47 ± 0.18	1.45 ± 0.22	1.6 ± 0.3	
		North	1.11 ± 0.13	5.4 ± 0.1	$\cdots$	$\cdots$	
LEDA 170194	C	Core	-0.09 ± 0.14	0.42 ± 0.17	-0.21 ± 0.14	-0.8 ± 0.4	
		SW	0.14 ± 0.24	1.9 ± 0.4	$\cdots$	$\cdots$	
		NE	0.7 ± 0.5	2.0 ± 0.9	$\cdots$	$\cdots$	
NGC 4593	A	core	-1.01 ± 0.15	-0.23 ± 0.16	0.77 ± 0.18	-0.54 ± 0.12	
IGR J13091+1137	A	core	-0.57 ± 0.16	-0.51 ± 0.19	2.6 ± 0.2	0.7 ± 0.4	
NGC 5252	A	core	0.04 ± 0.11	0.61 ± 0.17	0.28 ± 0.20	1.7 ± 0.1	
NGC 5506	D	core	0.95 ± 0.15	0.78 ± 0.11	1.1 ± 0.2	0.76 ± 0.11	
IGR J16385-2057	A	core	$\cdots$	$\cdots$	$\cdots$	0.74 ± 0.25	
IGR J17513-2011	A	core	-0.004 ± 0.140	-0.13 ± 0.18	0.9 ± 0.2	-0.40 ± 0.14	
IGR J18259-0706	A	core	0.86 ± 0.14	0.8 ± 0.2	-0.6 ± 0.4	0.07 ± 0.30	
2E 1853.7+1534	A	core	$\cdots$	$\cdots$	$\cdots$	$\cdots$	
IGR J20186+4043	A	core	0.87 ± 0.14	0.44 ± 0.17	1.3 ± 0.2	0.9 ± 0.3	
4C +74.26	A	core	-0.15 ± 0.09	0.003 ± 0.200	0.24 ± 0.20	0.7 ± 0.1	
IGR J23308+7120	A	core	0.64 ± 0.30	-0.4 ± 0.4	$\cdots$	$\cdots$	
IGR J23524+5842	B	core	-0.6 ± 0.2	0.65 ± 0.20	4.63 ± 0.34	$\cdots$	
		NE	1.33 ± 0.40	1.8 ± 0.7	$\cdots$	$\cdots$	

as pre-upgrade observations (like the ones concerning work cited before) were characterised by higher RMS with respect to post-upgrade observations[7] (like the ones presented here), which translates into different flux limits and therefore different detection rates. A proper comparison, although only at higher frequencies, can be carried out with the 22 GHz, 1-arcsec characterisation of SWIFT/BAT hard-X-ray selected AGN made by Smith et al. (2016, 2020), in which they re-port a high ($\sim 96/100$) detection rate, compatible with our estimate within the uncertainty at the same frequency.

As reported in Paper I, the detection rate of radio emission at high frequencies is larger than what has been reported in recent studies about mm emission in a handful of RQ AGN (e.g. Behar et al. 2015, 2018). Moreover, if we compare with the results obtained for LLAGN only, then our detection rates are larger not only at the higher frequencies (e.g. Doi et al. 2011), but also at the lower ones (see for comparison e.g. Ho & Ulvestad 2001; Saikia et al. 2018; Chiaraluce et al. 2019).

[7] The post-upgrade VLA can reach 4 μJy beam^{-1} (1-σ, in 1 hour) continuum sensitivity at most bands, one order of magnitude lower than pre-upgrade VLA (e.g. van Moorsel 2014)
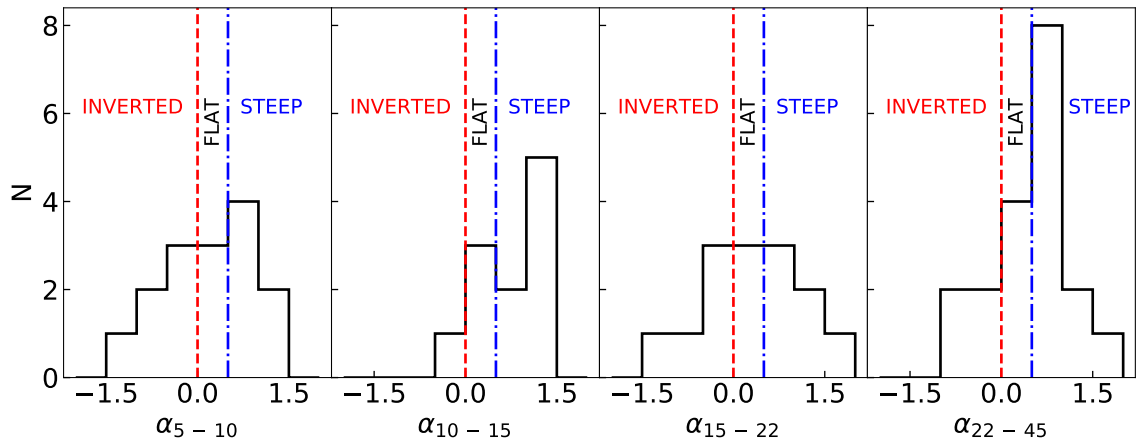
Figure 5. Histogram showing the distribution of two-bands spectral indices ($S_\nu^I \propto \nu^{-\alpha}$) for the core components of sources in this work; i.e. α_{5-10}, α_{10-15}, α_{15-22} and α_{22-45} from left to right. The region with $\alpha < 0$ and delimited by the red dashed line represents the 'inverted' regime; the region with $0 < \alpha < 0.5$ between the red dashed and the blue dot-dashed lines represents the 'flat' regime; the region with with $\alpha > 0.5$ and delimited by the blue dot-dashed line represents the 'steep' regime, according to the adopted definitions.

5.2 Morphology

According to the morphological classification presented in the previous section, we find a prevalence of compact sources, either unresolved/slightly resolved (17/28, ∼61 per cent), with the remaining sources exhibiting jet-like features, as well as triple and more complex morphologies.

Previous surveys on Seyfert galaxies have found morphologies in similar proportions, in which however the relative fraction depends on the frequency band, as the detection fraction of extended structures is higher at low frequencies, while the fraction of compact ones increases at higher frequencies (e.g. Ulvestad et al. 1981; van der Hulst et al. 1981; Kukula et al. 1998; Nagar et al. 1999; Leipski et al. 2006; Baldi et al. 2018, 2021a). Gallimore et al. (2006) found that, for a sample of Seyfert galaxies observed at 5 GHz with compact (D) configuration of the VLA (therefore lower angular resolution ∼15-20 arcsec) the fraction of sources exhibiting kiloparsec-scale radio structures (KSRs) is significantly higher (∼45 per cent). They suggest that the lower fraction of extended sources found in a number of works (e.g. Ulvestad & Wilson 1989; Kukula et al. 1995; Schmitt et al. 2001; Thean et al. 2001) may be due to the high resolution, which resolves out the extended, low-surface brightness, steep-spectrum emission, with the KSRs being likely associated to the nuclear AGN jet activity. For our sources presented here, it is not possible to rule out that in a number of them low-surface brightness emission, may be present as well.

In Smith et al. (2016, 2020), a compact component in all the detected sources is found. In more than a half (55/96) of the sample, this is the only component (either unresolved or slightly resolved), in agreement with our findings, while in 11/96 sources jet-like structures on sub-kpc to kpc scales are present. However, they find a significant number of sources (30/96) with a diffuse morphology (i.e. extended but non-linear), which they attribute to nuclear star formation.

5.3 Radio nuclear spectral energy distribution

The radio spectral slope in RQ AGN is likely the result of the combination of different emitting components dominating at different frequencies. Star-formation typically produces a synchrotron steep spectrum in the 1-10 GHz regime, while a compact core is characterized by a flat or inverted spectrum (Chen et al. 2022). An AGN wind/outflow and an extended jet produce an optically-thin synchrotron steep spectrum (Panessa et al. 2019).

In our sample, we find a prevalence of single power-law spectra, with the number of flat spectra equal to the number of steep spectra. If we include also single power-law sources with only two data points, then the flat spectra are 9 while the steep ones are 11.

In Fig. 6 we have plotted the mean spectral energy distribution obtained by calculating the mean of the slopes of the cores between two frequencies from Table 3 represented in F_ν in arbitrary units. The average trend is that of a nearly flat slope that steepens with increasing frequency, a major steepening is observed between 15 and 22 GHz. It is interesting to note that between 22 and 45 GHz the slope flattens again. This suggests that the core emission is generally optically thick below 15 GHz, in agreement with the results presented in (Laor et al. 2019) for quasars with a similar range of Eddington ratios. It becomes optically thin above 15 GHz and between 22 and 45 GHz it becomes optically thick again. If we assume that the emission is produced by synchrotron, the size of the emitting region at 15 GHz is smaller than the broad line region size (from eq.22 in Laor & Behar (2008)). At higher frequencies, another emitting source should be even smaller, as higher frequency emission originates at smaller radii, and the flat spectrum can be the result of the the emissivity integrated over the emitting volume. An increased radio emission is indeed expected if the observed 'mm-excess' component is extrapolated down to 45 GHz (Laor & Behar 2008; Behar et al. 2018).

Table 4. Results of the SED fitting for the sources in the sample. *Columns:* (1) Target name; (2) Component; (3) classification of core SED; (4) Spectral index from linear fit to all points; (5) Break frequency (in GHz) in case of broken power-law fit or peak in case of log-parabola fit; (6) Spectral index at $\nu \leqslant \nu_B$ (before break or peak); (7) Spectral index at $\nu \geqslant \nu_B$ (after break or peak). We show first the sources for which the core can be fitted by a broken power law, then those for which we performed a log-parabolic fit, finally the sources for which the core can be fitted by a single power-law. The sources for which only two data points or less were available (6/30) are omitted.

Target (1)	Comp (2)	SED class (3)	α_{All} (4)	$\nu_{Break/Peak}$ (5)	$\alpha(\nu \leqslant \nu_{Break/Peak})$ (6)	$\alpha(\nu \geqslant \nu_{Break/Peak})$ (7)
NGC 5252	Core	BPL	-	∼10	-0.04±0.11	+0.56±0.12
IGR J18259-0706	Core	BPL	-	∼15	0.77±0.03	0.03±0.09
QSO B0241+62	Core	BPL	-	∼15	-1.12±0.15	0.31±0.03
	Blob	-	-	∼10	0.57±0.13	2.4±0.2
NGC 1142	d	-	+0.97±0.04	-	-	-
	East	-	+0.76±0.09	-	-	-
	A1	-	+0.94±0.11	-	-	-
	A2	-	+1.25±0.25	-	-	-
	b (Core)	BPL	-	∼15	-0.09±0.05	+0.74±0.11
NGC 4593	Core	C-	-	∼15	-1.01±0.15	+0.8±0.2
	Excess	-	-0.54±0.12	-	-	-
IGR J13091+1137	Core	C-	-	∼10	-0.57±0.16	+2.6±0.2
	Excess	-	+0.7±0.4	-	-	-
IGR J23524+5842	Core	C-	-	∼9	-0.57±0.17	+4.6±0.3
	North	-	1.78±0.02	-	-	-
Mkn 50	Core	S	-0.02±0.02	-	-	-
NGC 5506	Core	S	+0.85±0.02	-	-	-
IGR J17513-2011	Core	S	+0.01±0.08	-	-	-
IGR J20186+4043	Core	S	+0.90±0.03	-	-	-
MGC+08-11-11	Core	S	+0.78±0.09	-	-	-
	Jet	-	-	-	-	-
LEDA 170194	Core	S	-0.10±0.08	-	-	-
	SW	-		∼10	+0.14±0.24	1.9±0.4
	NE	-		∼10	0.7±0.5	2.0±0.9
Mkn 3	West	S	1.22±0.07	-	-	-
	East (Core)	-	0.88±0.06	-	-	-
Mkn 6	North	-	+1.24±0.05	-	-	-
	South (Core)	S	+0.92±0.04	-	-	-
NGC 1068	d	-	+0.81±0.16	-	-	-
	a	-	+1.00±0.08	-	-	-
	b (Core)	S	+1.04±0.09	-	-	-
	SW	-	-	-	-	-
NGC 788	Core	S	+0.19±0.06	-	-	-
4C +74.26	Core	S	+0.23±0.13	-	-	-
B3 0309+411B	Core	S	-0.4±0.1	-	-	-
IGR J23308+7120	Core	S	+0.21±0.30	-	-	-
NGC 4388	NE (Core)	S	0.67±0.09	-	-	-
	SW	-	-	∼15	+0.68±0.08	+1.53±0.01

## 5.4 Radio - X-ray correlations

It has been found that both XRB and AGN follow tight X-ray versus radio luminosity correlations, with two different tracks, i.e. one characterised by a slope of ∼ 0.8 and followed by low-hard state XRB and low-luminosity AGN (LLAGN, e.g. Gallo et al. 2003; Salvato et al. 2004; Panessa et al. 2007; Chiaraluce et al. 2019), and one characterised by a slope of ∼ 1.4 and followed by 'outliers' XRB and bright RQ AGN (e.g. Coriat et al. 2011; Panessa et al. 2015; Dong et al. 2014). The scaling with the black-hole mass has led to the formulation of the 'fundamental' plane of black-hole activity (e.g. Merloni et al. 2003; Bonchi et al. 2013; Dong et al. 2014), and to theories unifying the accretion-ejection physics of XRB and AGN (e.g. Körding et al. 2006). Typically, a flat slope of ∼ 0.8 is associated to radiatively-inefficient accretion flows (e.g. Falcke et al. 2004; Coriat et al. 2011; Dong & Wu 2015), while a steep slope of ∼ 1.4 is associated to radiatively-efficient

accretion flows (e.g. Coriat et al. 2011; Gallo et al. 2012; Fender & Gallo 2014; Dong et al. 2014; Qiao & Liu 2015).

In Table 5 we summarise the results of the correlations between the peak radio luminosities of the core components and the X-ray ones. In Fig. 7 we show the plots of the corresponding correlations (left panel). Since in 22 and 45 GHz bands censored data in the peak radio luminosities were present, in order to estimate the slopes we used the EM algorithm in the Astronomy Survival Analysis software package ASURV Rev 1.2 (Isobe et al. 1990; Lavalley et al. 1992), which implements the methods presented in Isobe et al. (1986).

In order to strengthen the validity of the radio versus X-ray correlation, we have checked the significance of the corresponding flux-flux correlations. In Table 1 in Supplementary material we report the statistical values associated to flux-flux relations, and they are plotted in Fig. 1 in Supplementary material. The radio versus 2-10 keV flux-flux relations
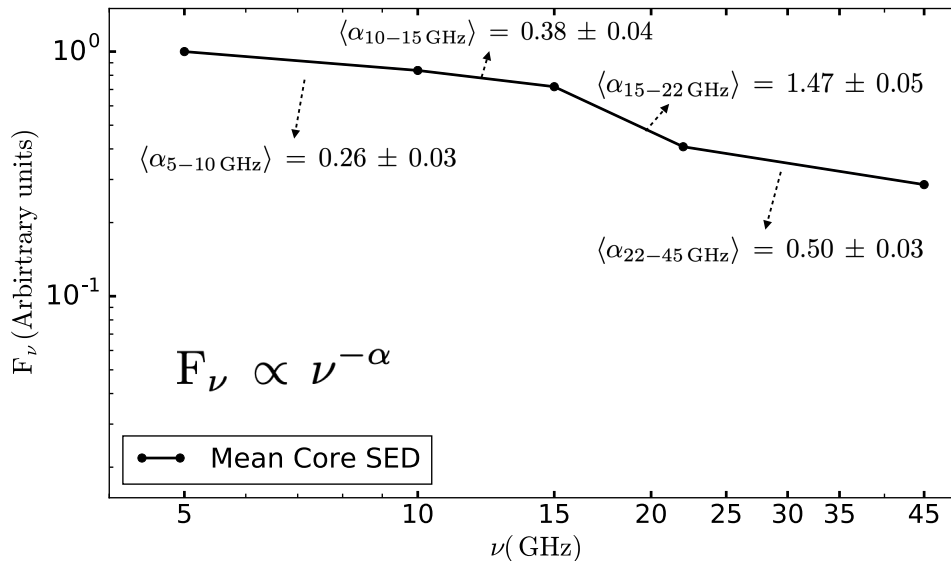
Figure 6. Mean nuclear Spectral Energy Distribution in F_ν between 5 and 45 GHz obtained by calculating the mean of the two frequencies spectral slopes of the cores reported in Table 3 and plotted in arbitrary units.

are strong ($r \sim 0.6 - 0.8$) and significant ($P \leqslant 10^{-3}$), while in the case in which 20-100 keV fluxes are considered the significance is lower ($\sim 10^{-2}$).

The slopes of the luminosity-luminosity relations at all frequencies (blue dashed lines in the plots), except at 10 GHz, are compatible with the slope of 1.4 found in the case of radiatively efficient sources, with high correlations coefficients and significance at 5 and 15 GHz, while at 22 and 45 GHz, where upper limits are present, the correlations are weaker and the significance is lower (order $\sim 10^{-3}$).

In Fig. 7, the well known powerful radio sources previously mentioned occupy a different locus. For this reason we investigated the same correlations excluding the 'Offset' sources (red dot-dashed lines). The slopes obtained in this case tend to be flatter with respect to the previous case, with values in the range 0.6 - 1.2 and, although the correlations are strong ($r \sim 0.6$ - 0.8), the significance of the relations is lower, i.e. $\sim 10^{-3}$. This is expected, as the powerful radio sources occupy the high-luminosity region of the plane with the result of driving the overall relation (e.g. Hardcastle et al. 2009).

We investigated also the existence of correlations between the peak radio luminosity and hard-X-ray (i.e. 20-100 keV) one (right panel of Fig. 7), finding strong correlations ($\rho = 0.5$-0.7) with slopes in the range 1.3-2, with a high significance (order of $\sim 10^{-3} - 10^{-4}$). When the 'offset' sources are excluded, in analogy with radio-X-ray correlations, the slope flatten ($\sim 0.6 - 1.1$) and, although strong ($\rho = 0.8$-0.6), the significance is lower ($\sim 10^{-2}$).

The slopes of the radio-X-ray luminosity correlations are compatible with 1.4 found by Panessa et al. (2015) using the complete sample of 79 hard X-ray selected Seyferts and 1.4 GHz data ($\sim 10\%$ of RL sources are present in their sample). However, the radio observations in Panessa et al. (2015)

are at 1.4 GHz and have a resolution of ~ 45 arcsec, much larger than ours. Therefore, the flux densities and luminosities considered for the relation may be contaminated by contribution from extended, off-nuclear component, which may be not directly AGN-related. Moreover, they consider all the 79 Seyferts in the sample of Malizia et al. (2009), including several powerful radio sources. Our slopes are also consistent with the findings presented in Dong et al. (2014) for a sample of bright RQ AGN with similar properties (i.e. Eddington ratios larger than 1 per cent and relatively low redshift, $z \leqslant 0.3$), compatible with a radiatively-efficient accretion regime as postulated in AGN-XRB unification theories. However, when powerful radio sources are excluded, the slopes become flatter. The peak of the distribution of Eddington ratios of the sources in our work is in the range between -2.25 and -1.5, while that of Dong et al. (2014), is in the range between -1 and -0.5. Our result would suggest that when intermediate accretion regimes are considered, the slope of the relation flattens, with values which are intermediate between the 0.8 slope for the very-low accretion regimes and the slope of 1.4 for higher accretion regimes.

With these observations we can test if the sources follow the empirical $L_R/L_X \sim 10^{-5}$ relation valid for coronally-active stars. The finding that also bright RQ AGN follow the relation has been interpreted in light of models in which both radio and X-ray would come from a hot corona (e.g. Laor & Behar 2008). In the left panel of Fig. 7 the solid black line represents the above relation. We find that at 5 and 10 GHz the sources, except for the offset ones, roughly follow the relation, but at higher frequencies (15, 22 and 45 GHz) their peak radio luminosities tend to be systematically above the relation. In order to quantify this effect, we calculated mean values of
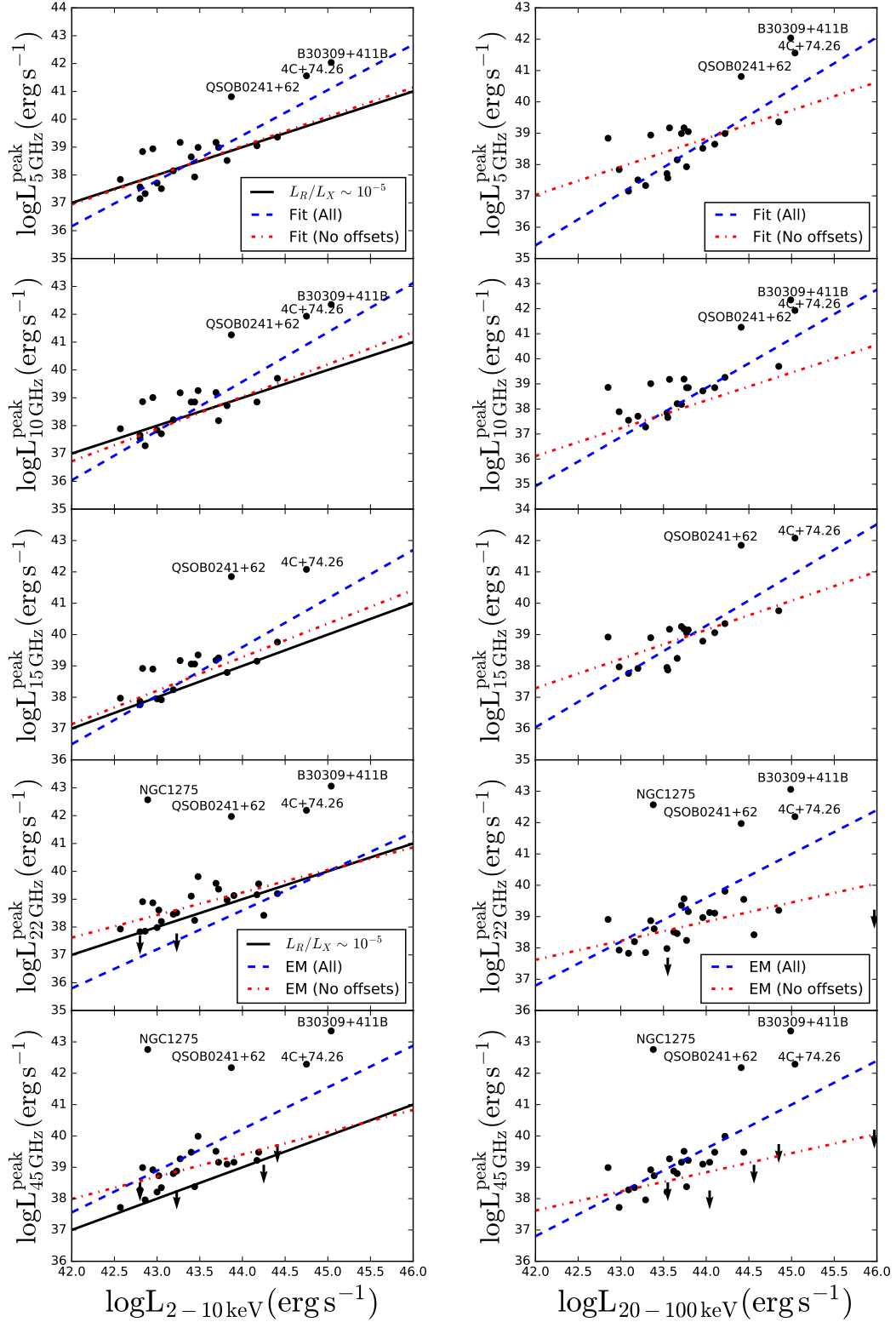
Figure 7. Plots of the correlations between peak radio luminosities of the core components and X-ray (2-10 keV, left panel) and hard-X-ray (20-100 keV, right panel) ones. From top to bottom: 5, 10, 15, 22 and 45 GHz bands. The solid black line is the $L_R/L_X \sim 10^{-5}$ relation; the dashed blue line represents a regression considering all the data, the red dot-dashed line represents a regression discarding the offset sources (i.e. QSO B0241+62, B3 0309+411B, NGC 1275 and 4C +74.26, see the text). In the case of 22 and 45 GHz bands, since upper limits were present, the regression lines are calculated from a EM algorithm.

the quantity $\log L_R/L_X$ for the non-offset sources[8], considering different radio luminosities, with the KMESTM routine in the ASURV package[9]. The mean values are -4.9±0.1 at 5 GHz, -4.8±0.1 at 10 GHz, -4.6±0.1 at 15 Ghz, -4.8±0.1 at 22 GHz and -4.5±0.1 at 45 GHz[10], with an increase of $\log L_R/L_X$ ratio with frequency. We note that the $\log L_R/L_X$ relation has been found considering the 5 GHz luminosity (e.g. Laor & Behar 2008), while Behar et al. (2018) found that when high frequencies (i.e. at ~ 100 GHz) are considered, the relation rather follow a $\sim 10^{-4}$ trend. Indeed, we find that as the frequency increases, the sources tend to cluster in this intermediate regime.

There is still no definite explanation for the observed functional form of relation and care should be taken when deriving physical conclusions based on them. Indeed, several works reported that different slopes are found when considering different classes of objects, i.e. only RL sources (Wang et al. 2006), Giga-Hertz Peaked and Compact Steep Spectrum sources (GPS and CSS, e.g. Fan & Bai 2016), Narrow-Line Seyfert 1 (NLS1, e.g. Yao et al. 2018), and blazars (Zhang et al. 2018). Magnetically dominated coronae may explain the observed relations in RQ AGN (e.g. Laor & Behar 2008, and references therein). Alternatively, an interpretation in terms of a coupling of inflow and outflow as in XRBs may apply (e.g. Carotenuto et al. 2021, and references therein).

6 CLUES ON THE ORIGIN OF NUCLEAR RADIO EMISSION

Four sources in our sample are well known powerful radio emitters QSO B0241+62, B3 0309+411B, NGC 1275 and 4C +74.26. Their radio properties are consistent with the jet activity already reported by previous studies (e.g. Hutchings et al. 1982; de Bruyn 1989; Pedlar et al. 1990; Ho & Ulvestad 2001; Healey et al. 2007; Lister et al. 2019; Bruni et al. 2020).

The remaining sources (26/30) can be classified as RQ considering their radio properties. Two of them are undetected (IGR J16426+6536 and IGR J18027-1455) and one of them (2E 1853.7+1534) has been detected at 22 GHz (only 22 and 45 GHz observation were available) resulting in a diffuse component that maybe consistent with jet/outflow or starburst emission.

Steep spectra are found in 11/30 sources. Five of them, namely NGC 1068, MCG+08-11-11, Mkn 3, Mkn 6 and NGC 4388, exhibit resolved, jet-like structure, sometimes coupled to more complex features. For these sources, the origin of observed radio emission is compatible with optically-thin synchrotron emission from a sub-relativistic jet. This in agreement with previous studies reporting aligned structures on mas scales, high-brightness temperature ($\gg 10^8$ K) and flat spectrum for the mas cores (e.g. Kukula et al. 1996, 1999; Lal et al. 2004). However, in NGC 1068 and NGC 4388, while

a jet is observed at kpc and sub-kpc scales, mas scales observations revealed low brightness temperature cores ($\sim 10^5$ K), compatible with thermal free-free emission from the inner torus (e.g. Gallimore et al. 1996; Kukula et al. 1999; Mundell et al. 2000; Giroletti & Panessa 2009). Six sources, namely NGC 4151, IGR J00333+6122, LEDA 168563, NGC 5506, IGR J1638-2057 and IGR J20186+4043, exhibit a compact morphology and a steep spectrum. In this case, the observed radio emission may be due to optically-thin emission from a sub-relativistic jet which is unresolved by our observations, as already observed in NGC 4151 and NGC 5506 (e.g. Pedlar et al. 1993; Mundell et al. 2003; Middelberg et al. 2004; Ulvestad et al. 2005). Radio emission from star formation may instead occur at larger (a few kpc) scales (e.g. Padovani et al. 2011; Condon et al. 2013). For the remaining sources optically-thin synchrotron emission from disc winds can not be ruled out and higher resolution observations are needed.

Three sources, namely IGR J23524+5842, NGC 4593 and IGR J13091+1137, exhibit peaked spectra in the GHz range. The source IGR J23524+5842 exhibits a core coupled to a one-sided lobe, and its radio emission likely comes from a jet; for the other two this hypothesis can not be confirmed, as they are compact and the SED exhibits an additional component at high frequencies.

Two more sources, namely NGC 5252 and NGC 1142, exhibit cores with flat spectra up to a break (at $\sim$10 and $\sim$15 GHz, respectively). This emission is likely due to a jet, the subsequent spectral decline is probably marking the transition to the optically-thin regime. In the former, the non-thermal origin of radio emission has been confirmed by VLBI studies (e.g. Mundell et al. 2000), while in the latter this scenario cannot be confirmed. The extra-nuclear radio emission of NGC 1142 is of star formation origin and it is discussed in a dedicated section in Appendix A.

Finally, seven sources, namely NGC 788, 4U 0517+17, Mkn 50, LEDA 170194, IGR J17513-2011, IGR J18259-0706 and IGR J23308+7120, exhibit compact flat-spectrum cores. In addition to the flat core, LEDA 170194 shows a steep-spectrum two-sided jet extending over $\sim$2 kpc.

The observed radio sources above exhibit flat spectra up to 45 GHz (with the exception of IGR J23308+7120, which is flat up to 15 GHz and undetected at 22 and 45 GHz). This may be due to optically-thick synchrotron emission from a compact jet. However, flat radio spectra extending up to high frequencies, may also be due to synchrotron radio emission from a magnetically-heated corona (e.g. Laor & Behar 2008). In the so-called coronal models, the corona is a radially-stratified plasma, both in the magnetic field and number density of relativistic electrons, in either a spherical or disc geometry. Each plasma shell emits as optically-thick synchrotron radiation, but variations in the opacity from one shell to another produce different turnover frequencies, such that external shells dominate low frequencies, while inner ones dominate the high frequency range. The result is an overall flat radio spectrum (e.g. Raginski & Laor 2016). One difference between the compact jet and coronal emission scenario is that in the former a break in the spectral slope (due to the optically-thick/optically-thin transition) is expected at relatively low frequencies (a few tens of GHz), while the compactness of the corona can result in flat spectra up to $\sim$ 300 GHz (e.g. Laor & Behar 2008; Raginski & Laor 2016). This suggests that, with the resolution and frequency cover-

---

[8] The offset sources, as expected, are characterised by $\log L_R/L_X, \geqslant -3$

[9] The routine KMESTM gives the Kaplan-Meier estimator for the distribution function of a randomly censored sample

[10] In the case in which the smallest value is an upper limit the mean may suffer from statistical biases, for details see the ASURV documentation.

Table 5. Results of the correlation between peak radio luminosities of the core components and the 2-10 keV luminosities, for all the sample and excluding the offset sources. Associated flux-flux correlations are also reported. *Columns:* (1) the relation; (2) sample considered; (3) the slope of the relation (log-log); (4) the intercept; (5) Spearmnan's rank correlation coefficient; (6) probability of the null hypothesis that null hypothesis is that two sets of data are uncorrelated; (7) Kendall's tau; (8) probability of the null hypothesis.
(*) For K and Q bands, since upper limits in the dependent variables were present, the reported values are from the EM regression algorithm, the Spearman's rho and the Generalised Kendall's tau calculated in the ASURV package.

Relation	Sample	m (slope)	q (intercept)	ρ (Spearman)	P-value (Spearman)	τ (Kendall's)	P-value (Kendall's)
(1)	(2)	(3)	(4)	(5)	(6)	(7)	(8)
$\log L_{5\,GHz}^{peak} - \log L_{2-10\,keV}$	All	1.63±0.23	-32±10	0.8	9×10^{-6}	0.64	5×10^{-5}
	RQ	1.05±0.25	-7±11	0.7	1×10^{-3}	0.5	2×10^{-3}
$\log F_{5\,GHz}^{peak} - \log F_{2-10\,keV}$	All	1.33±0.42	-4±5	0.6	7×10^{-3}	0.4	6×10^{-3}
	RQ	1.33±0.40	-4±5	0.6	7×10^{-3}	0.4	7×10^{-3}
$\log L_{10\,GHz}^{peak} - \log L_{2-10\,keV}$	All	1.77±0.24	-38±10	0.7	2×10^{-4}	0.6	3×10^{-4}
	RQ	1.16±0.25	-12±11	0.6	1×10^{-2}	0.4	1×10^{-2}
$\log F_{10\,GHz}^{peak} - \log F_{2-10\,keV}$	All	1.36±0.42	-3±5	0.64	2×10^{-3}	0.5	3×10^{-3}
	RQ	1.37±0.40	-3±5	0.6	2×10^{-3}	0.5	3×10^{-3}
$\log L_{15\,GHz}^{peak} - \log L_{2-10\,keV}$	All	1.55±0.30	-29±11	0.8	2×10^{-5}	0.6	1×10^{-4}
	RQ	1.07±0.20	-8±9	0.76	3×10^{-4}	0.6	1×10^{-3}
$\log F_{15\,GHz}^{peak} - \log F_{2-10\,keV}$	All	1.16±0.40	-5±5	0.6	7×10^{-3}	0.4	9×10^{-3}
	RQ	1.15±0.44	-5.4±4.9	0.6	7×10^{-3}	0.43	9×10^{-3}
$\log L_{22\,GHz}^{peak} - \log L_{2-10\,keV}{}^{*}$	All	1.4±0.4	-23±17	0.64	1×10^{-3}	z∼3.5	4×10^{-4}
	RQ	0.81±0.21	3.6±9.0	0.7	1.4×10^{-3}	z∼3.2	1.5×10^{-3}
$\log F_{22\,GHz}^{peak} - \log F_{2-10\,keV}{}^{*}$	All	1.4±0.5	-3±5	0.6	2×10^{-3}	z∼3.2	1×10^{-3}
	RQ	1.05±0.30	-6.8±3.0	0.6	5×10^{-3}	z∼3.17	1.5×10^{-3}
$\log L_{45\,GHz}^{peak} - \log L_{2-10\,keV}{}^{*}$	All	1.33±0.40	-18±17	0.6	3×10^{-3}	z∼3.4	7×10^{-4}
	RQ	0.71±0.2	8±8	0.6	6×10^{-3}	z∼3.04	2×10^{-3}
$\log F_{45\,GHz}^{peak} - \log F_{2-10\,keV}{}^{*}$	All	1.4±0.5	-3±6	0.6	2×10^{-3}	z∼3.3	1×10^{-3}
	RQ	1.0±0.3	-7.4±3.0	0.6	4×10^{-3}	z∼3.23	1×10^{-3}

age of our observations, the external layers of the corona are eventually sampled.

In order to put more stringent constraints to the origin of radio emission in these sources VLBI observations will be fundamental. Indeed, it will be possible to determine the mas size of the sources, as a size smaller than ∼pc rules out star-formation or an AGN wind interacting with the interstellar medium. Moreover, it will also exclude free-free emission, as a brightness temperature much larger than $\sim 10^6$ K is compatible only with non-thermal emission (e.g. Condon & Ransom 2016). Finally, variability studies can constrain the size of the emitting regions and therefore discriminate between star formation and non-thermal emission, like the base of a jet or a corona, expected to vary on relatively small timescales (e.g. Barvainis et al. 2005; Baldi et al. 2015; Panessa et al. 2022).

7 CONCLUSIONS

In this paper we presented wide-band (5 - 45 GHz), high-sensitivity (a few μJy beam^{-1}), sub-arcsec (1-0.4″) JVLA observations for a sample of 30 nearby ($0.003 \leqslant z \leqslant 0.3$) and moderately accreting ($-2.5 \leqslant \log L/L_{Edd} \leqslant -0.5$) hard-X-ray selected AGN. The observations allow to characterise the sub-kpc scale radio properties of the sample and build wide-band SEDs, with the final aim of investigating the origin of radio emission. Below we summarise our main findings:

• We find a high detection fraction of radio emission at all frequencies, that decreases with frequency (21/21, 21/21, 19/19, 26/29 and 24/29, i.e. 96, 96, 95, 87 and 81 per cent at 5, 10, 15, 22 and 45 GHz, respectively). These values occupy

the high tail of the distribution of the detection rates reported in literature for RQ AGN, typically around 70 - 90 per cent.

• The radio luminosities of the detected sources are in the range between $37 \leqslant \log L_R (erg\,s^{-1}) \leqslant 40$. Four sources are known powerful radio emitters and indeed show larger luminosities $\geqslant 41$ (in log units).

• Two sources (observed only at 22 and 45 GHz) have not been detected. The upper limits on their flux densities are ∼0.15 and 0.1 mJy beam^{-1}. One of them, IGR J16426+6536, has been observed twice, ∼17 months apart, in both cases it is undetected. The upper limits on radio luminosities imply values of the X-ray radio-loudness $R_X < -4.5$, at the very-low-power tail of radio-loudness distribution, possibly hinting to a 'radio-silent' nature.

• The morphology of the sources varies with the selected frequency, where extended emission dominates the lower frequencies. Overall, the majority of them are compact, characterised by a core component (17/30). The remaining sources exhibit either one-sided (7/30) or two sided (1/30) jets. Three sources exhibit a complex morphology.

• The SED of the sources can be classified into three categories: single power-law spectra (14/30), convex spectra (3/30) and broken power law spectra (4/30). For 6/30 sources only 2 SED data points (at 22 and 45 GHz) are available, while for one source only one data point is available. We derive a mean radio spectral energy distribution of the cores.

• We find a significant radio-X-ray correlation at all frequencies. When the four powerful radio emitters are excluded, the slopes of the correlation range between m = 0.7 − 1.2. This range is intermediate between the slope of 1.4 found for high luminosity AGN and the slope of 0.8 found for LLAGN,

in agreement with the intermediate accretion rates and luminosities covered by the sample considered here.

• Our sources roughly follow the empirical Gudel-Benz relation, with a transition from the 10^{-5} to the 10^{-4} relation at higher frequencies (i.e. 15, 22 and 45 GHz), suggesting a possible contribution to both radio and X-ray from a hot corona. The four powerful radio emitters significantly depart from the relation, as expected.

The combination of morphology, SED shape and (when available) VLBI information from the literature allows to formulate possible scenarios for the radiative mechanisms responsible for the radio emission: i) ∼13% of the sample is RL; ii) ∼37% of the sample has steep spectra compatible with optically-thin synchrotron from a jet, which is unresolved in compact cores. In ∼13% of them, optically-thin synchrotron from disc winds can not be ruled out; iii) flat spectrum sources are generally compact (except for LEDA 170194 which exhibits a two-sided jet), indicating a possible optically-thick synchrotron emission from a compact jet and/or a hot corona (∼30%); iv) in ∼30% of the sample, peaked core spectra are found (in one case showing a one-sided jet morphology) again suggesting a possible jet scenario.

This work is part of a large project aiming at investigating the origin of radio emission through high-resolution, high-sensitivity, multi epoch, wide-band radio observations. Our volume limited, well characterized hard X-ray sample is perfectly suited to push over this effort by exploiting the unprecedented capabilities of the Square Kilometer Arrays (SKA) pathfinders and precursors.

DATA AVAILABILITY

The data underlying this article were accessed from NRAO (https://science.nrao.edu/). The derived data generated in this research will be shared on reasonable request to the corresponding author.

REFERENCES

Aghanim, N., Akrami, Y., Ashdown, M., et al. 2018, Planck 2018 results. VI. Cosmological parameters

Antonucci, R. & Barvainis, R. 1988, ApJl, 332, L13

Appleton, P. N., Charmandaris, V., Gao, Y., Jarrett, T., & Bransford, M. A. 2003, ApJ, 586, 112

Baldi, R. D., Behar, E., Laor, A., & Horesh, A. 2015, MNRAS, 454, 4277

Baldi, R. D., Laor, A., Behar, E., et al. 2022, MNRAS, 510, 1043

Baldi, R. D., Williams, D. R. A., Beswick, R. J., et al. 2021a, MNRAS, 508, 2019

Baldi, R. D., Williams, D. R. A., McHardy, I. M., et al. 2018, MNRAS, 476, 3478

Baldi, R. D., Williams, D. R. A., McHardy, I. M., et al. 2021b, MNRAS, 500, 4749

Barvainis, R., Lehár, J., Birkinshaw, M., Falcke, H., & Blundell, K. M. 2005, ApJ, 618, 108

Barvainis, R., Lonsdale, C., & Antonucci, R. 1996, AJ, 111, 1431

Bassani, L., Venturi, T., Molina, M., et al. 2016, MNRAS, 461, 3165

Behar, E., Baldi, R. D., Laor, A., et al. 2015, MNRAS, 451, 517

Behar, E., Vogel, S., Baldi, R. D., Smith, K. L., & Mushotzky, R. F. 2018, MNRAS, 478, 399

Bonchi, A., La Franca, F., Melini, G., Bongiorno, A., & Fiore, F. 2013, MNRAS, 429, 1970

Briggs, D. S. 1995, in Bulletin of the American Astronomical Society, Vol. 27, American Astronomical Society Meeting Abstracts, 1444

Bruni, G., Panessa, F., Bassani, L., et al. 2020, MNRAS, 494, 902

Calzetti, D., Kennicutt, R. C., Engelbracht, C. W., et al. 2007, ApJ, 666, 870

Carotenuto, F., Corbel, S., Tremou, E., et al. 2021, MNRAS, 505, L58

Chen, S., Stevens, J. B., Edwards, P. G., et al. 2022, MNRAS, 512, 471

Chiaraluce, E., Bruni, G., Panessa, F., et al. 2019, MNRAS, 485, 3185

Chiaraluce, E., Panessa, F., Bruni, G., et al. 2020, MNRAS, 495, 3943

Condon, J. J. 1992, ARA&A, 30, 575

Condon, J. J., Helou, G., Sanders, D. B., & Soifer, B. T. 1990, ApJs, 73, 359

Condon, J. J., Kellermann, K. I., Kimball, A. E., Ivezić, Ž., & Perley, R. A. 2013, ApJ, 768, 37

Condon, J. J. & Ransom, S. M. 2016, Essential Radio Astronomy

Coriat, M., Corbel, S., Prat, L., et al. 2011, MNRAS, 414, 677

de Bruyn, A. G. 1989, AAP, 226, L13

Doi, A., Nakanishi, K., Nagai, H., Kohno, K., & Kameno, S. 2011, AJ, 142, 167

Dong, A.-J. & Wu, Q. 2015, MNRAS, 453, 3447

Dong, A.-J., Wu, Q., & Cao, X.-F. 2014, ApJl, 787, L20

Falcke, H., Körding, E., & Markoff, S. 2004, AAP, 414, 895

Falcke, H., Malkan, M. A., & Biermann, P. L. 1995, AAP, 298, 375

Fan, X.-L. & Bai, J.-M. 2016, ApJ, 818, 185

Fender, R. & Gallo, E. 2014, SSR, 183, 323

Ferrarese, L. & Merritt, D. 2000, ApJl, 539, L9

Ferreira, J. & Deguiran, R. 2013, High Energy Density Physics, 9, 67

Gallimore, J. F., Axon, D. J., O'Dea, C. P., Baum, S. A., & Pedlar, A. 2006, AJ, 132, 546

Gallimore, J. F., Baum, S. A., O'Dea, C. P., & Pedlar, A. 1996, ApJ, 458, 136

Gallo, E., Fender, R. P., & Pooley, G. G. 2003, MNRAS, 344, 60

Gallo, E., Miller, B. P., & Fender, R. 2012, MNRAS, 423, 590

Gao, Y., Solomon, P. M., Downes, D., & Radford, S. J. E. 1997, ApJl, 481, L35

Giroletti, M. & Panessa, F. 2009, ApJl, 706, L260

Gültekin, K., Richstone, D. O., Gebhardt, K., et al. 2009, ApJ, 698, 198

Hardcastle, M. J., Evans, D. A., & Croston, J. H. 2009, MNRAS, 396, 1929

Healey, S. E., Romani, R. W., Taylor, G. B., et al. 2007, ApJs, 171, 61

Hippelein, H. H. 1989, AAP, 216, 11

Ho, L. C. & Ulvestad, J. S. 2001, ApJs, 133, 77

Högbom, J. A. 1974, A&AS, 15, 417

Hutchings, J. B., Campbell, B., Gower, A. C., Crampton, D., & Morris, S. C. 1982, APJ, 262, 48

Isobe, T., Feigelson, E. D., Akritas, M. G., & Babu, G. J. 1990, ApJ, 364, 104

Isobe, T., Feigelson, E. D., & Nelson, P. I. 1986, ApJ, 306, 490

Jiang, Y.-F., Ciotti, L., Ostriker, J. P., & Spitkovsky, A. 2010, ApJ, 711, 125

Joy, M. & Ghigo, F. D. 1988, ApJ, 332, 179

Kellermann, K. I., Sramek, R., Schmidt, M., Shaffer, D. B., & Green, R. 1989, AJ, 98, 1195

Körding, E., Rupen, M., Knigge, C., et al. 2008, Science, 320, 1318

Körding, E. G., Jester, S., & Fender, R. 2006, MNRAS, 372, 1366

Kormendy, J. & Richstone, D. 1995, ARA&A, 33, 581

Kukula, M. J., Dunlop, J. S., Hughes, D. H., & Rawlings, S. 1998, MNRAS, 297, 366

Kukula, M. J., Ghosh, T., Pedlar, A., & Schilizzi, R. T. 1999, ApJ, 518, 117

Kukula, M. J., Holloway, A. J., Pedlar, A., et al. 1996, MNRAS, 280, 1283

Kukula, M. J., Pedlar, A., Baum, S. A., & O'Dea, C. P. 1995, MNRAS, 276, 1262

Lal, D. V., Shastri, P., & Gabuzda, D. C. 2004, AAP, 425, 99

Lamb, S. A., Hearn, N. C., & Gao, Y. 1998, ApJl, 499, L153

Laor, A., Baldi, R. D., & Behar, E. 2019, MNRAS, 482, 5513

Laor, A. & Behar, E. 2008, MNRAS, 390, 847

Lavalley, M., Isobe, T., & Feigelson, E. 1992, in Astronomical Society of the Pacific Conference Series, Vol. 25, Astronomical Data Analysis Software and Systems I, ed. D. M. Worrall, C. Biemesderfer, & J. Barnes, 245

Leipski, C., Falcke, H., Bennert, N., & Hüttemeister, S. 2006, AAP, 455, 161

Lister, M. L., Homan, D. C., Hovatta, T., et al. 2019, ApJ, 874, 43

Magorrian, J., Tremaine, S., Richstone, D., et al. 1998, AJ, 115, 2285

Malizia, A., Stephen, J. B., Bassani, L., et al. 2009, MNRAS, 399, 944

McMullin, J. P., Waters, B., Schiebel, D., Young, W., & Golap, K. 2007, in Astronomical Society of the Pacific Conference Series, Vol. 376, Astronomical Data Analysis Software and Systems XVI, ed. R. A. Shaw, F. Hill, & D. J. Bell, 127

Merloni, A., Heinz, S., & di Matteo, T. 2003, MNRAS, 345, 1057

Mezcua, M., Roberts, T. P., Sutton, A. D., & Lobanov, A. P. 2013, MNRAS, 436, 3128

Middelberg, E., Roy, A. L., Nagar, N. M., et al. 2004, AAP, 417, 925

Morganti, R. 2017, Frontiers in Astronomy and Space Sciences, 4, 42

Mundell, C. G., Wilson, A. S., Ulvestad, J. S., & Roy, A. L. 2000, ApJ, 529, 816

Mundell, C. G., Wrobel, J. M., Pedlar, A., & Gallimore, J. F. 2003, ApJ, 583, 192

Nagar, N. M., Falcke, H., Wilson, A. S., & Ulvestad, J. S. 2002, AAP, 392, 53

Nagar, N. M., Wilson, A. S., Mulchaey, J. S., & Gallimore, J. F. 1999, ApJs, 120, 209

Nyland, K., Dong, D. Z., Patil, P., et al. 2020, ApJ, 905, 74

Padovani, P. 2016, AAPr, 24, 13

Padovani, P., Miller, N., Kellermann, K. I., et al. 2011, ApJ, 740, 20

Panessa, F., Baldi, R. D., Laor, A., et al. 2019, Nature Astronomy, 3, 387

Panessa, F., Barcons, X., Bassani, L., et al. 2007, AAP, 467, 519

Panessa, F., Bassani, L., Cappi, M., et al. 2006, AAP, 455, 173

Panessa, F. & Giroletti, M. 2013, MNRAS, 432, 1138

Panessa, F., Pérez-Torres, M., Hernández-García, L., et al. 2022, MNRAS, 510, 718

Panessa, F., Tarchi, A., Castangia, P., et al. 2015, MNRAS, 447, 1289

Pedlar, A., Ghataure, H. S., Davies, R. D., et al. 1990, MNRAS, 246, 477

Pedlar, A., Kukula, M. J., Longley, D. P. T., et al. 1993, MNRAS, 263, 471

Perley, R. A. & Butler, B. J. 2017, ApJs, 230, 7

Price, D. J., Pringle, J. E., & King, A. R. 2003, MNRAS, 339, 1223

Qiao, E. & Liu, B. F. 2015, MNRAS, 448, 1099

Raginski, I. & Laor, A. 2016, MNRAS, 459, 2082

Robitaille, T. & Bressert, E. 2012, APLpy: Astronomical Plotting Library in Python

Roy, A. L., Colbert, E. J. M., Wilson, A. S., & Ulvestad, J. S. 1998, ApJ, 504, 147

Saikia, P., Körding, E., Coppejans, D. L., et al. 2018, AAP, 616, A152

Salvato, M., Greiner, J., & Kuhlbrodt, B. 2004, ApJl, 600, L31

Sánchez, S. F., Kennicutt, R. C., Gil de Paz, A., et al. 2012, AAP, 538, A8

Sauro, J. & Lewis, J. R. 2005, Proceedings of the Human Factors and Ergonomics Society Annual Meeting, 49, 2100

Scheuer, P. A. G. & Williams, P. J. S. 1968, ARA&A, 6, 321

Schmitt, H. R., Antonucci, R. R. J., Ulvestad, J. S., et al. 2001, ApJ, 555, 663

Sebastian, B., Kharb, P., O'Dea, C. P., Gallimore, J. F., & Baum, S. A. 2020, MNRAS, 499, 334

Silpa, S., Kharb, P., Ho, L. C., et al. 2020, MNRAS, 499, 5826

Smith, K. L., Mushotzky, R. F., Koss, M., et al. 2020, MNRAS, 3237

Smith, K. L., Mushotzky, R. F., Vogel, S., Shimizu, T. T., & Miller, N. 2016, ApJ, 832, 163

Terashima, Y. & Wilson, A. S. 2003, ApJ, 583, 145

Thean, A., Pedlar, A., Kukula, M. J., Baum, S. A., & O'Dea, C. P. 2000, MNRAS, 314, 573

Thean, A. H. C., Gillibrand, T. I., Pedlar, A., & Kukula, M. J. 2001, MNRAS, 327, 369

Ulvestad, J. S. & Wilson, A. S. 1986, MNRAS, 218, 711

Ulvestad, J. S. & Wilson, A. S. 1989, ApJ, 343, 659

Ulvestad, J. S., Wilson, A. S., & Sramek, R. A. 1981, ApJ, 247, 419

Ulvestad, J. S., Wong, D. S., Taylor, G. B., Gallimore, J. F., & Mundell, C. G. 2005, AJ, 130, 936

van der Hulst, J. M., Crane, P. C., & Keel, W. C. 1981, AJ, 86, 1175

van Moorsel, G. 2014, in 2014 XXXIth URSI General Assembly and Scientific Symposium (URSI GASS), 1–3

Wang, R., Wu, X.-B., & Kong, M.-Z. 2006, ApJ, 645, 890

Wilson, A. S. & Colbert, E. J. M. 1995, ApJ, 438, 62

Yao, S., Qiao, E., Wu, X.-B., & You, B. 2018, MNRAS, 477, 1356

Zakamska, N. L. & Greene, J. E. 2014, MNRAS, 442, 784

Zakamska, N. L., Lampayan, K., Petric, A., et al. 2016, MNRAS, 455, 4191

Zhang, X., Zhang, H., & Zhang, X. 2018, APSS, 363, 259

Zirbel, E. L. & Baum, S. A. 1995, ApJ, 448, 521

Zubovas, K. 2019, MNRAS, 483, 1957

APPENDIX A: NGC 1142

NGC 1142 is a massive spiral galaxy and is part of an interacting system *Arp 118*, in which the companion is the massive elliptical galaxy NGC 1143, ∼40 arcsec far away in the NW direction (∼24 kpc). It is most probably the result of a collisional encounter (e.g. Joy & Ghigo 1988).

Its radio map exhibits a complex morphology, with a central component, named B, where the core is believed to reside, plus additional extra-nuclear components on scales of ∼10 kpc (total extension). At 5, 10 and 15 GHz, a southern ridge of radio emission extending on approximately the same spatial scale is visible. At 22 GHz 6 components are detected plus a southern ridge, namely East, A1, A2, C, B and D. In the 45 GHz naturally-weighted map only three components are detected, namely A1, A2 and B. This is due to a combined effect of the steep spectrum of the off-nuclear components and the lower sensitivity at 45 GHz with respect to 22 GHz. At 5 GHz (archival post-upgrade JVLA observations) the East component is blended with A1, while the C component is not detected. At 10 and 15 GHz the significance of the detection of the off-nuclear components is lower. This is due to a combined effect of the steep spectrum and the higher RMS in these bands with respect to 5 and 22 GHz maps (archival VLA observations were of lower sensitivity before the upgrade). The observed morphology is compatible with previous radio studies at comparable resolution (e.g. Joy & Ghigo 1988; Condon et al. 1990; Thean et al. 2000), although an additional component, C, is detected with a high significance at 22 GHz.

The present observations at matched resolution, although with slightly different sensitivities, allow to build for the first time the SED for all the detected components. The core (component B) exhibit a spectrum which is flat/inverted up to to a break occurring at ∼15 GHz, with a steep decline after it (see Table 4). This likely originates from the base of a jet, However, due to the missing information at the mas scale, it is not possible to rule out a possible thermal origin.

The extra-nuclear components are characterised by steep spectra in cm/sub-cm range, with spectral indices in the range 0.7-1.3 (see Table 4 and bottom-right panel of Fig. 4). These values, together with the observed morphology, are compatible with radio emission from star formation (e.g. Condon 1992; Panessa et al. 2019). This source is part of the Calar Alto Legacy Integral Field spectroscopy Area (CALIFA) survey (Sánchez et al. 2012) which covers the range of 3700 - 7000 angstrom with a 3.7 arcsec resolution.

In Fig. A1 we show over-plots of 22 GHz contours with optical emission lines images corresponding to different lines, i.e. NII, OII, Hα and Hβ (the corresponding wavelengths of each optical map are indicated on top). These lines may trace recent star formation (e.g. Calzetti et al. 2007). From Fig. A1 it is possible to make the following considerations: i) the component B, the nucleus, is always optically bright, as expected; ii) the component D is bright in all emission lines; iii) the southern ridge is bright in NII, OII and Hα, it is weak in Hβ; iv) the triple group East/A1/A2 is bright in OII, it is weak in Hα, β and NII.

The above considerations are suggesting that the radio emission from the extra-nuclear steep spectrum components, coinciding with spikes in optical emission lines maps, is indeed synchrotron radiation from regions of intense star formation, as first proposed by Joy & Ghigo (1988). Previous works support this interpretation and have found that the component D indeed coincides with a giant HII region (e.g. Hippelein 1989); the southern ridge is part of the ring of the disk galaxy which is stripped in an elliptical geometry because of encounter with the companion galaxy, which has produced an enhancement in the molecular gas density, as traced by CO(1-0) observations (Gao et al. 1997, e.g.). In this scenario, the coincidence of star forming regions traced by optical and radio observations with regions of increased gas density is supported by dynamical models (e.g. Lamb et al. 1998). While the interpretation of the origin of steep-spectrum radio emission of the extra-nuclear components D and southern ridge fits with the above picture, that of triple East/A1/A2 is not straightforward, as it appears weak in emission lines (except for OII) and it is spatially coincident with a gap in the molecular gas CO(1-0) (Gao et al. 1997). Interpretations for the origin of this radio emission comprise emission from SNR in molecular gas clouds with low density (e.g. Gao et al. 1997), radio emission from star formation triggered by the temporary enhanced density in the impact locus (e.g. Lamb et al. 1998) or emission from cosmic rays from star formation and supernovae explosions (e.g. Appleton et al. 2003).
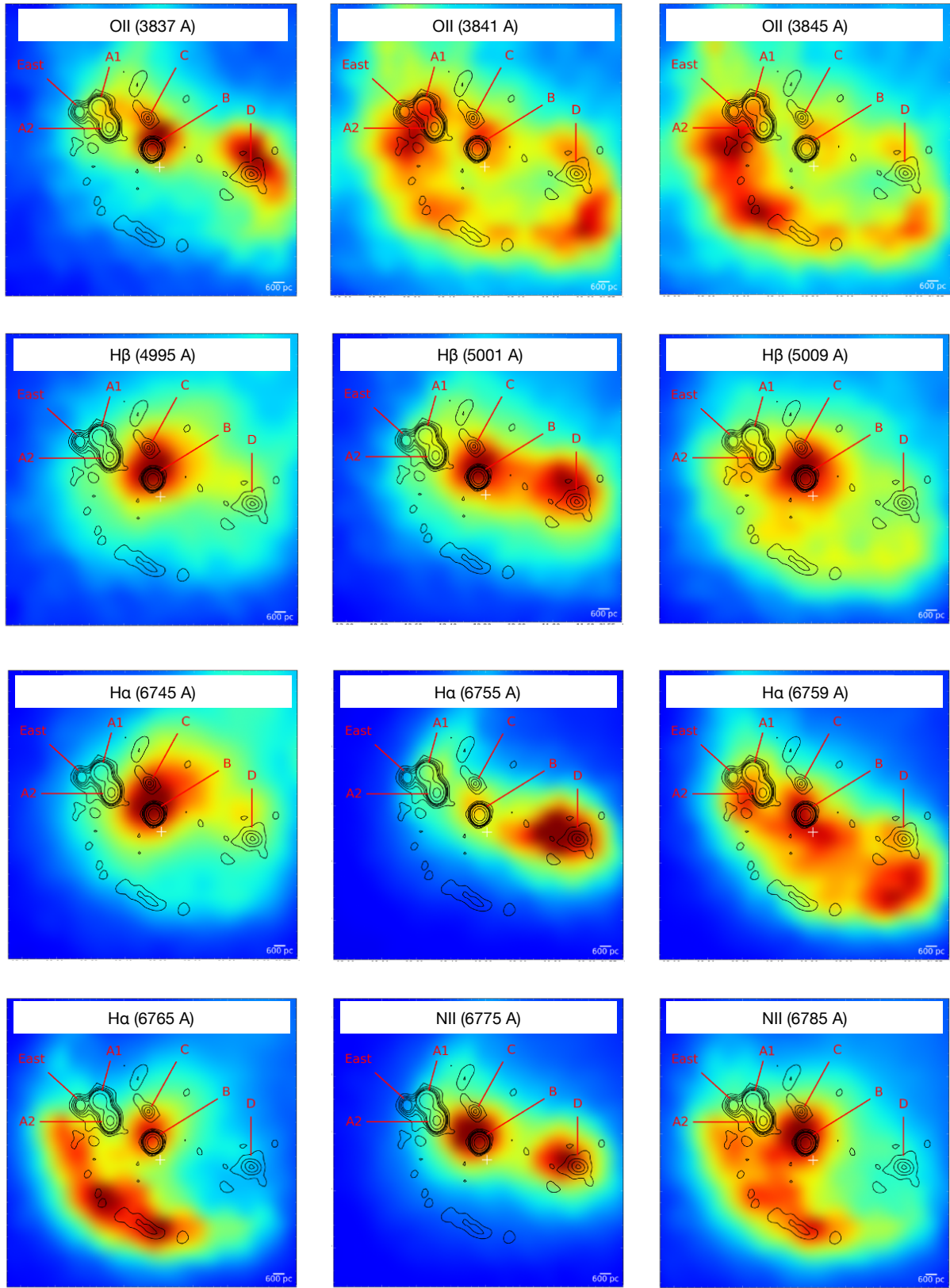
Figure A1. Maps for NGC 1142 in which we overplot our proprietary K-band contours to CALIFA emission lines maps at different wavelengths, comprising OII, Hβ, Hα and NII. In each map, the wavelength corresponding to the optical emission line image is indicated (in angstroms).